

pubs.acs.org/cm Article

Ultralow Thermal Conductivity and High Thermopower in a New Family of Zintl Antimonides $Ca_{10}MSb_9$ (M = Ga, In, Mn, Zn) with Complex Structures and Heavy Disorder

Alexander Ovchinnikov, Sevan Chanakian, Alexandra Zevalkink, and Svilen Bobev*



Cite This: Chem. Mater. 2021, 33, 3172-3186



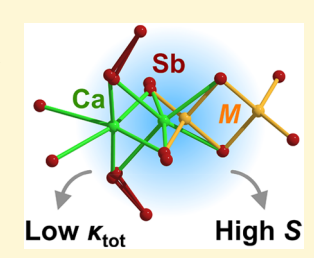
ACCESS

Metrics & More

Article Recommendations

Supporting Information

ABSTRACT: A new family of Zintl antimonides with the approximate composition $Ca_{10}MSb_9$ (M = Ga, In, Mn, Zn) has been obtained via two synthetic approaches: (1) using Sb as a flux and (2) using the conventional high-temperature method in welded Nb tubes. The new compounds crystallize in a disordered variant of the tetragonal $Ca_{10}LiMgSb_9$ structure type. The observed occupational and positional disorder serves as a means to retain a charge-balanced composition, which ultimately results in semiconducting behavior, predicted from first-principles and measured experimentally. High-temperature transport measurements reveal ultralow thermal conductivity $(0.5-0.7 \text{ W} \cdot \text{m}^{-1} \cdot \text{K}^{-1})$, due to the extensive disorder, and high values of the Seebeck coefficient $(100-200 \ \mu\text{V} \cdot \text{K}^{-1})$ at $T = 800 \ \text{K}$). The highest thermoelectric figure of merit, zT = 0.2, exhibited by the In representative without any optimization, suggests that good thermoelectric performance can be achieved in this family of compounds.



1. INTRODUCTION

Efficient and sustainable production of energy is one of the most important objectives of the modern society. One of the ways to provide economic and environmentally friendly use of energy is recovery of waste heat, produced in the course of natural or industrial processes, operation of vehicles, and so on. Thermoelectric materials are capable of harvesting energy by converting heat into electricity. The efficiency of such materials is characterized by a dimensionless figure of merit, zT, defined as $zT = S^2T/\rho\kappa$, where S, T, ρ , and κ are the thermopower (also called the Seebeck coefficient), absolute temperature, electrical resistivity, and total thermal conductivity, respectively. In general, optimization of thermoelectric performance is a challenging task due to the mutual correlation of the physical quantities in this equation. 1,2 For instance, decreasing the electrical resistivity by injection of charge carriers inevitably increases the electronic part of the thermal conductivity, $\kappa_{\rm e}$.

A special class of materials that has been actively explored as promising candidates for thermoelectric applications are Zintl phases—valence-precise intermetallic compounds with polar chemical bonding. The charge balance in these materials is achieved by electron redistribution between different parts of the crystal structure so that the constituting atoms adopt a stable closed-shell electron configuration. Typically, such compounds demonstrate semiconducting properties with narrow electronic bandgaps and tunable electrical resistivity. At the same time, high structural complexity enables low phonon group velocities and efficient phonon scattering and hence low thermal conductivity. The same time and the

Most Zintl phases of relevance for thermoelectric research belong to the chemical families of tetrelides and pnictides, i.e., compounds with the elements of groups 14 and 15, respectively. One of the highest-performing materials within the pnictide family is $Yb_{14}MnSb_{11}$, with the maximum zT value approaching 1.2 at $T \ge 1000$ K. $^{12-14}$ Other notable Zintl pnictides with promising thermoelectric performance include Mg_3Sb_2 , $^{15-17}$ AEM_2Pn_2 (AE = alkaline-earth metal, Yb, Eu; M = Mg, Mn, Zn, Cd; Pn = Sb, Bi), $^{18-30}$ AE_3MSb_3 (AE = Ca, Sr; M = Al, Ga), $^{31-33}$ $AE_5M_2Sb_6$ (AE = Ca, Sr; M = Al, Ga), $^{34-39}$ BaGa $_2Sb_2$, 40 $AMSb_4$ (A = K, Rb, Cs; M = Al, Ga), $^{41-43}$ and $A_9M_{4+x}Sb_9$ (A = Ca, Yb; M = Zn, Mn). $^{44-47}$ Electrical transport properties of these materials are usually tuned by suitable chemical doping, 13,47,48 while thermal conductivity can be reduced by introduction of crystallographic disorder. 28,49,50

In this contribution, we report on the discovery and detailed characterization of a new family of ternary antimonides with the general simplified formulas $Ca_{10}MSb_9$ (M=Ga, In, Mn, and Zn). The latter represents an approximate composition with integer numbers that can be ascribed to the actual $Ca_{10+x+y}M_{1-y}Sb_9$ (0 < x < 0.5, 0 < y < 0.7, with the values of x and y being a function of the nature of x0. The apparent optimal number of valence electrons in these compounds allows them to be classified as Zintl phases. The charge balance is achieved by development of extensive crystallographic disorder, which also contributes to the very low thermal conductivity. In combination with high thermopower and semiconducting behavior, these new materials can be suggested

Received: December 29, 2020 Revised: March 20, 2021 Published: April 5, 2021





Table 1. Refinement Details and Selected Crystallographic Data from the Four SCXRD Data Collections for $Ca_{10+x+y}M_{1-y}Sb_9$ ($\sim Ca_{10}MSb_9$, M = Ga, In, Mn, Zn)^a

refined formula	$Ca_{10.91(1)}Ga_{0.38(1)}Sb_{9} \\$	$Ca_{11.01(2)}In_{0.35(1)}Sb_9$	$Ca_{10.82(2)}Zn_{0.66(1)}Sb_9$	$Ca_{10.48(1)}Mn_{1.09(2)}Sb_9$
composition from EDX	$Ca_{10.6(2)}Ga_{0.7(1)}Sb_{9}$	$Ca_{10.5(1)}In_{0.6(1)}Sb_9$	$Ca_{10.7(2)}Zn_{0.8(1)}Sb_{9}$	$Ca_{10.5(1)}Mn_{1.0(1)}Sb_9$
fw/g·mol ⁻¹	1559.37	1577.56	1572.30	1575.57
a/Å	11.8911(4)	11.924(2)	11.830(2)	11.923(1)
c/Å	17.1962(6)	17.186(3)	17.246(3)	16.931(2)
$V/{ m \AA}^3$	2431.5(2)	2443.4(9)	2413.3(8)	2406.9(6)
$ ho_{ m calc}/{ m g}{ m \cdot cm}^{-3}$	4.26	4.29	4.33	4.35
$\mu_{ ext{MoK}lpha}/ ext{cm}^{-1}$	125.3	124.1	128.3	127.0
$R_{ m int}$	0.040	0.100	0.074	0.071
$R_1 \left[I > 2\sigma_{(I)} \right]^b$	0.021	0.042	0.034	0.032
$wR_2 \left[I > 2\sigma_{(I)}\right]^b$	0.043	0.083	0.068	0.064
R_1 [all data] b	0.022	0.062	0.047	0.044
wR_2 [all data] b	0.044	0.090	0.072	0.067
$\Delta ho_{ m max,min}/{ m e}\cdot{ m \AA}^{-3}$	0.86, -1.44	1.59, -1.27	1.58, -1.24	1.06, -1.27

^αAll structures are with the space group $P4_2/mnm$, Z=4, and the data are collected at T=200 K using Mo Kα radiation ($\lambda=0.71073$ Å). ${}^bR_1=\sum ||F_0|-|F_0|/\sum |F_0|$; $wR_2=[\sum [w(F_0^2-F_c^2)^2]/\sum [w(F_0^2)^2]]^{1/2}$, where $w=1/[\sigma^2F_0^2+(AP)^2+(BP)]$ and $P=(F_0^2+2F_c^2)/3$. A and B are the respective weight coefficients (see the CIF data).

Table 2. Atomic Coordinates and Equivalent Isotropic Displacement Parameters (Å²) for Ca_{10.82(2)}Zn_{0.66(1)}Sb₉

atom	site	\boldsymbol{x}	y	z	$U_{ m eq}^{\;\;a}$	occupancy ^b
Ca1	16k	0.0121(1)	0.2503(1)	0.18815(8)	0.0154(3)	1
Ca2	16k	0.0154(1)	0.3387(1)	0.39611(8)	0.0152(3)	1
Ca3	4 <i>g</i>	0.1750(2)	\overline{x}	0	0.0147(6)	1
Ca4	4 <i>f</i>	0.1646(9)	\boldsymbol{x}	0	0.029(3)	0.343(5)
Ca5	4 <i>f</i>	0.3087(4)	\boldsymbol{x}	0	0.018(2)	0.48(1)
Ca6	4e	0	0	0.3533(2)	0.0211(7)	1
Zn1	4 <i>f</i>	0.1044(2)	\boldsymbol{x}	0	0.0179(8)	0.657
Sb1	8 <i>j</i>	0.22323(4)	\boldsymbol{x}	0.31895(4)	0.0144(2)	1
Sb2A	8 <i>j</i>	0.3035(7)	\boldsymbol{x}	0.1637(5)	0.0135(6)	0.343
Sb2B	8 <i>j</i>	0.3144(3)	\boldsymbol{x}	0.1785(2)	0.0135	0.657
Sb3A	8 <i>i</i>	0.0060(4)	0.3564(4)	0	0.0120(4)	0.343
Sb3B	8 <i>i</i>	0.0387(2)	0.3277(2)	0	0.0120	0.657
Sb4	4 <i>g</i>	0.37360(6)	\overline{x}	0	0.0217(3)	1
Sb5	4e	0	0	0.12600(5)	0.0137(2)	1
Sb6	4d	0	1/2	1/4	0.0101(2)	1

 $^{a}U_{\rm eq}$ is defined as one-third of the trace of the orthogonalized $U_{\rm ij}$ tensor. Anisotropic displacement parameters were kept equal within the atomic pairs Sb2A/Sb2B and Sb3A/Sb3B, respectively. b The following constraints were used for the site occupancies (occ): occ(Ca4) = occ(Sb2A) = occ(Sb3A) = 1 - occ(Zn1) = 1 - occ(Sb2B) = 1 - occ(Sb3B).

as suitable candidates for further systematic optimization of their thermoelectric performance.

2. EXPERIMENTAL SECTION

2.1. Synthesis. Single crystals of $Ca_{10}MSb_9$ (M = Ga, In, Mn) were grown from an Sb flux. Elemental Ca, M, and Sb (Alfa, all with stated purity >99.9 wt %) were loaded in a 2 mL alumina crucible with the ratio Ca/M/Sb = 2:1:5. The crucible was topped with a piece of quartz wool and sealed in an evacuated fused silica tube. The reactor was then placed in a box furnace, heated up to 1273 K with a rate of 200 K/h, kept at this temperature for 10 h, and cooled down to 1023 K with a rate of 5 K/h. At that point, the tube was taken out from the furnace, and the Sb flux was immediately separated by centrifugation. Note that high-temperature centrifugation is associated with a risk of quartz reactor implosion and must be performed with proper personal protective equipment: fireproof clothing, heatresistant gloves, and a face shield. After the tube was opened in the glovebox, irregularly shaped crystals were found inside the alumina crucible. The size of the crystals was usually limited by the crucible dimensions (several mm), suggesting that even larger crystals can be obtained by this method. The high M content in the starting mixture

was necessary to obtain the desired $Ca_{10}MSb_9$ crystals. Ca-richer melts always yielded the binary phase $Ca_{11}Sb_{10}$ as the main product.

The Sb flux technique was not applicable for the growth of $Ca_{10}ZnSb_9$. Different synthetic protocols always resulted in single crystals of $Ca_{11}Sb_{10}^{51}$ or $Ca_9Zn_{4+x}Sb_9^{52,53}$ Reactions with molten Zn as a flux usually produced single crystals of $CaZn_2Sb_2^{29,54}$ We also tried crystal growth from molten Pb, since the Pb flux technique has been recently shown to be an efficient method for the preparation of yet another new ternary compound in the discussed system, $Ca_{14}Zn_{1+x}Sb_{11}^{55}$ which is difficult to access by other synthetic routes. Elemental Ca, Zn, Sb, and Pb were mixed in the ratio 10:1:9:15, respectively. The rest of the procedure was similar to the protocol described above for the Sb flux method, but the employed dwelling temperature was lowered to 1173 K, to avoid losses of the volatile Zn metal, and the centrifugation temperature was 873 K. Although we were able to prepare single crystals of $Ca_{10}ZnSb_9$ by this technique, their small size and the presence of some residual Pb flux hindered detailed physical property measurements.

Powder samples were produced by high-temperature reaction of the respective elements with proper stoichiometric ratios. These experiments were based on the actual refined compositions of $Ca_{10+x+y}M_{1-y}Sb_9$ ($\sim Ca_{10}MSb_9$, M=Ga, In, Mn, Zn), which are represented in Table 1. The elements were loaded in Nb tubes in the

Table 3. Atomic Coordinates and Equivalent Isotropic Displacement Parameters (Å²) for Ca_{10.48(1)}Mn_{1.09(2)}Sb₉

atom	site	\boldsymbol{x}	y	z	$U_{ m eq}^{a}$	occupancy
Ca1	16k	0.0075(1)	0.2508(1)	0.18987(9)	0.0170(3)	1
Ca2	16k	0.0119(1)	0.3374(1)	0.39733(9)	0.0149(3)	1
Ca3	4 <i>g</i>	0.1778(2)	\overline{x}	0	0.0174(7)	1
Ca4	4 <i>f</i>	0.1681(4)	\boldsymbol{x}	0	0.023(2)	0.475(3)
Ca5	4e	0	0	0.3590(2)	0.0217(7)	1
Mn1	4 <i>f</i>	0.0923(3)	\boldsymbol{x}	0	0.016(1)	0.525
Mn2	4 <i>f</i>	0.2648(2)	\boldsymbol{x}	0	0.013(2)	0.506(8)
Mn3	4 <i>f</i>	0.377(3)	\boldsymbol{x}	0	0.013	0.045(5)
Sb1	8 <i>j</i>	0.22068(4)	\boldsymbol{x}	0.31871(4)	0.0162(2)	1
Sb2A	8 <i>j</i>	0.304(2)	\boldsymbol{x}	0.162(2)	0.016(2)	0.475
Sb2B	8 <i>j</i>	0.314(2)	\boldsymbol{x}	0.169(2)	0.016	0.525
Sb3A	8i	0.0067(3)	0.3561(3)	0	0.0132(4)	0.475
Sb3B	8 <i>i</i>	0.0337(3)	0.3211(2)	0	0.0132	0.525
Sb4	4g	0.36858(6)	\overline{x}	0	0.0195(3)	1
Sb5	4e	0	0	0.13036(6)	0.0203(3)	1
Sb6	4 <i>d</i>	0	1/2	1/4	0.0121(2)	1

 $^{a}U_{\text{eq}}$ is defined as one-third of the trace of the orthogonalized U_{ij} tensor. Anisotropic displacement parameters were kept equal within the atomic pairs Mn2/Mn3, Sb2A/Sb2B, and Sb3A/Sb3B, respectively. b The following constraints were used for the site occupancies (occ): occ(Ca4) = occ(Sb2A) = occ(Sb3A) = 1 - occ(Mn1) = 1 - occ(Sb2B) = 1 - occ(Sb3B).

following manner: for M = Ga and In, Ca/M/Sb = 10.9:0.4:9; Ca/Mn/Sb = 10.5:1:9, Ca/Zn/Sb = 10.8:0.7:9.

The Nb containers were weld-shut under 600 mbar of high-purity Ar using an arc-welding facility and sealed in evacuated fused silica tubes, which were in turn loaded in tube furnaces. Temperature was ramped up to 1173 K with a rate of 200 K/h, where the materials were annealed for 96 h. Subsequently, the temperature was lowered to 293 K with a rate of 100 K/h. Powder X-ray diffraction analysis confirmed the phase purity of the obtained samples (Figure S1). The as-prepared polycrystalline samples were used for spark plasma sintering and subsequent high-temperature electrical and thermal transport measurements.

Single crystals of the title compounds were found to be stable in dry air over a period of at least several weeks. A visible tarnishing of the crystal surfaces suggests a formation of some passivating layer, which precludes further sample deterioration. Finely ground powder samples are more hygroscopic and should be stored under inert conditions.

2.2. Powder X-ray Diffraction (PXRD). PXRD patterns were taken on a Rigaku Miniflex and a Rigaku Smartlab diffractometer (Cu $K\alpha$ radiation, $\lambda=1.5418$ Å). LeBail refinements were performed with the Jana2006 program ⁵⁶ and were used to confirm the sample purity. For most samples, reliable Rietveld refinements were not feasible due to the high complexity of the crystal structures and preferred orientation effects. However, we employed constrained refinements for analysis of the sintered samples (Figure S2). For these calculations, atomic coordinates and occupancies were fixed at the values determined from single-crystal X-ray diffraction. A small amount of Ca_4Sb_2O , formed due to oxidation in the course of the sintering process and/or postsintering treatment, was included in the

2.3. Single-Crystal X-ray Diffraction (SCXRD). Single crystals were selected under dry Paratone-N oil. Suitable crystals were cut to desired dimensions and mounted on low-background plastic loops for measurements. Diffraction data were recorded in a stream of cold nitrogen at $T=200~\rm K$ on a Bruker SMART APEX CCD diffractometer equipped with monochromated Mo Kα radiation ($\lambda=0.71073~\rm \AA$). Data integration and absorption corrections were accomplished with the SAINT⁵⁷ and SADABS⁵⁸ software packages, respectively. Crystal structures were solved by dual-space methods as implemented in SHELXT⁵⁹ and refined by full matrix least-squares methods on F^2 with SHELXL.⁶⁰ Atomic coordinates were standardized using the STRUCTURE TIDY program.⁶¹ Details of the data collection and other relevant crystallographic parameters are given in Tables 1–3 and Tables S1–S7 in the Supporting Information. CIFs

have been deposited with the CCDC database with reference numbers 2048884–2048888.

2.4. Scanning Electron Microscopy. Semiquantitative compositional analysis of the flux-grown crystals and polycrystalline chunks extracted from the reactions in Nb tubes was conducted utilizing energy-dispersive X-ray spectroscopy (EDX) on an Auriga 60 CrossBeam Scanning Electron Microscope equipped with an Oxford Synergy X-MAX80 silicon drift detector. The samples were mounted on a carbon tape glued to a copper holder. The beam current and accelerating potential were 10 μ A and 20 kV, respectively, and the counting time for each spot was 60 s. Within the accuracy of the EDX method, the compositions of the crystals prepared by the flux-growth technique, and those selected from the reactions in Nb tubes were consistent with each other.

2.5. First-Principles Calculations. Electronic structure calculations on the density functional theory (DFT) level were carried out for an idealized Ca11ZnSb9 model. The structure was first fully optimized using the Vienna Ab initio Simulation Package (VASP). Exchange and correlation were described in the generalized-gradient approximation (GGA) with the Perdew-Burke-Ernzerhof exchangecorrelation functional (PBE).⁶³ The plane wave energy cutoff was set to 500 eV, and the Brillouin zone was sampled by a $3 \times 3 \times 2$ k-point grid. The forces were relaxed to less than 0.02 eV/Å. The optimized model was subsequently analyzed with the full-electron TB-LMTO-ASA code.⁶⁴ The von Barth-Hedin version of the local density approximation exchange-correlation functional (LDA) was employed.⁶⁵ To satisfy the atomic sphere approximation (ASA), the introduction of empty spheres was accomplished with the built-in procedure of the LMTO code. The Brillouin zone was sampled by a 6 \times 6 \times 4 k-point grid after checking for convergence. Chemical bonding was examined using crystal orbital Hamilton population curves (COHP),666 evaluated with the dedicated module of the LMTO software.

2.6. Physical Property Measurements. 2.6.1. Resistivity. Temperature-dependent electrical resistivity measurements were carried out for flux-grown crystals of $Ca_{10}MSb_9$ (M=Ga, In, Mn) on a Quantum Design Physical Property Measurement System (PPMS) in the temperature range 5–300 K using a standard four-probe technique. The crystals were gently polished with sandpaper to remove traces of the Sb flux. After that, electrical contacts were attached with a conductive silver paint. The measurements were done on cooling and heating to ensure reproducibility.

2.6.2. Magnetization. The temperature-dependence of the magnetization for a Ca_{10.5}MnSb₉ single crystal was measured on the PPMS in external fields between 0.5 and 70 kOe within the

temperature range 3–300 K. The measured sample (ca. 50 mg) was loaded in a low-background gel-cap holder and secured with quartz wool tips. High-temperature magnetization measurements were done on a Quantum Design Vibrating Sample Magnetometer (VSM) in an external field of 10 kOe in the temperature range 300–950 K. The crystal was immobilized using a Zircar alumina cement. After the measurements, the crystals were ground and analyzed with PXRD to confirm that no decomposition had occurred during the measurements.

2.6.3. Spark Plasma Sintering (SPS). Samples prepared in Nb tubes were pulverized through 10 min of ball milling with two 1/2" stainless steel ball bearings in stainless steel SPEX vials. The resulting powder was sintered under vacuum via spark plasma sintering (SPS, Dr. Sinter SPS-211LX) at 873 K for 10–20 min. We should note that the sintered pellets were found to be very air-sensitive, with surface oxidation visible within seconds. Measures were taken to reduce exposure to air/humidity to prevent oxidation during sintering and characterization.

2.6.4. High-Temperature Transport Characterization. Bulk polycrystalline samples with >95% of the theoretical density were used for all high-temperature transport measurements. High-temperature measurements were carried out under dynamic vacuum. Temperature-dependent resistivity was measured using a custom four-point probe van der Pauw resistivity setup with tungsten electrodes.⁶⁷ High-temperature Seebeck coefficients were measured in a custom uniaxial instrument using W-Nb thermocouples and light-pipe heating.⁶⁸ The thermal diffusivity, D, was measured using the laser flash method (Netzsch LFA-457). The thermal conductivity, κ , was subsequently calculated from D and the respective geometric density, d, of the samples ($\kappa = DC_v d$, C_v is the heat capacity at constant volume). $C_v \approx C_p$ (heat capacity at constant pressure) was assumed, and the Dulong-Petit approximation for heat capacity was assigned to C_p. An approximate error of 5% can be assumed for the thermal diffusivity and electrical conductivity measurements, and 10% can be assumed for Seebeck.

3. RESULTS AND DISCUSSION

3.1. Synthesis. The Sb flux is employed for the single-crystal growth of intermetallic compounds less frequently than the more conventional metal fluxes, such as Sn and Pb. This may be related to the high melting point of Sb ($T_{\rm m}=904~{\rm K}$), which narrows down the useful temperature region for crystal growing and creates challenges for the flux separation by the habitually used centrifugation method. Nevertheless, by careful optimization of the experimental conditions, the Sb flux technique can yield high-quality single crystals, suitable for various characterization techniques. Some recent examples of intermetallic materials obtained in the form of single crystals from liquid Sb (or Sb-rich eutectic mixtures) include the kagome metals ${\rm CaV_3Sb_4}^{70}$ and ${\rm AV_3Sb_5}$ (${\rm A=K}$, Rb, Cs), the noble metal antimonide ${\rm La_6Pd_{2+x}Sb_{15}}$ with a multiband electronic behavior, and ${\rm Mg_3Sb_2}$ with promising thermoelectric performance.

Our initial exploratory studies in the Ca–M–Sb systems (M = Ga, In), employing the Sb flux technique, were aimed at the synthesis of Ca₁₁Sb₁₀ derivatives with a doping of the M metal in the Sb sites, by analogy with Ca₁₁In₂Bi₈, which was predicted by us to be a potentially interesting system for testing of thermoelectric performance.⁷⁵ An exciting outcome of these synthetic attempts was the discovery of the new ternary compounds with the approximate composition Ca₁₀MSb₉ (M = Ga, In). Having recognized the structural flexibility of the discussed phases, we attempted aliovalent substitutions of the M metal, which afforded the isotypic Ca₁₀MSb₉ with M = Mn and Zn; although, the latter could not be produced by the Sb flux approach but was synthesized from

a Pb flux. All four compounds are also accessible in the form of polycrystalline samples, prepared by high-temperature treatment of the respective elements (Figure S1).

Additionally, still preliminary work indicates that isostructural phases can be produced by substituting Yb for Ca, Bi for Sb, and with M = Al or Cd. This is suggesting that the herein reported compounds represent only a small part of a novel, rich structural family.

3.2. Crystal Structure. Powder X-ray diffraction patterns of the crushed flux-grown $Ca_{10}MSb_9$ crystals revealed a striking resemblance to typical diffractograms of the binary pnictide $Ca_{11}Sb_{10}$ (Ho₁₁Ge₁₀ structure type, space group I4/mmm, a = 11.70 Å, c = 17.19 Å^{51,76}). The patterns could be indexed using tetragonal unit cells with $a \approx 12$ Å and $c \approx 17$ Å (Figure 1),

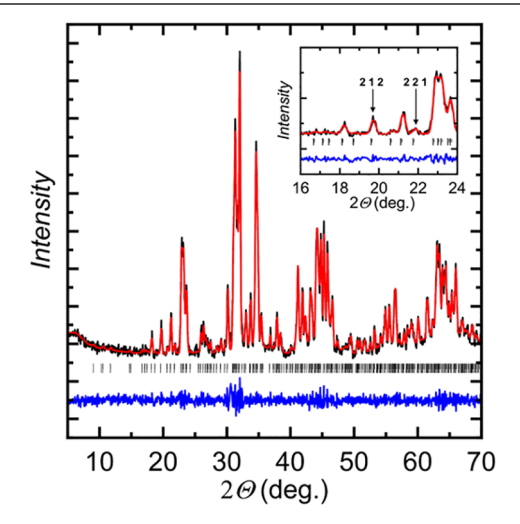


Figure 1. Powder X-ray diffraction pattern and a LeBail refinement in space group $P4_2/mnm$ of a crushed $Ca_{10}MnSb_9$ single crystal, $Cu\ K\alpha$ radiation, $\lambda=1.5418\ \text{Å}$. Experimental data, theoretical pattern, and difference curve are shown in black, red, and blue, respectively. Tick marks indicate the Bragg peak positions. Inset: An enlarged view of the pattern in the region $2\theta=16-24^\circ$. Arrows emphasize some intense reflections that would be forbidden in space group I4/mmm, adopted by the structurally related binary phase $Ca_{11}Sb_{10}$.

slightly different from those of the $Ca_{11}Sb_{10}$ archetype. At this point, the variation in the a- and c-parameters could have been attributed to incorporation of M-element into the "11-10" structure, in analogy to the substitutional derivate of $Ca_{11}Bi_{10}$, $Ca_{11}In_2Bi_8$. However, upon a closer look, several intense reflections can be seen to violate the extinction conditions of space group I4/mmm (h + k + l = 2n), which points instead toward the existence of a primitive unit cell with the said periodicity constants (Figure 1, inset).

Detailed analysis of the extinctions in the single-crystal X-ray diffraction data suggested three possible space groups: $P4_2nm$ (#102), $P\overline{4}n2$ (#118), and $P4_2/mnm$ (#136). Generation of the initial model was successful in the centrosymmetric space $P4_2/mnm$. Already at the early stages of the refinement, it was clear that the structures exhibit substantial crystallographic disorder, which could not be eliminated by reducing the symmetry. The disorder patterns in $Ca_{10}MSb_9$ are very similar for M=Ga, In, and Zn, with some peculiarities for M=Mn. For this reason, below, we will discuss in detail both the crystal structures of the Zn and Mn representatives.

It is convenient to start the discussion by deriving the crystal structure of " $Ca_{10}ZnSb_{9}$ " from that of the crystallographically

related binary pnictide Ca₁₁Sb₁₀, adopting the Ho₁₁Ge₁₀ structure type (space group *I4/mmm*, Figure 2, top). The

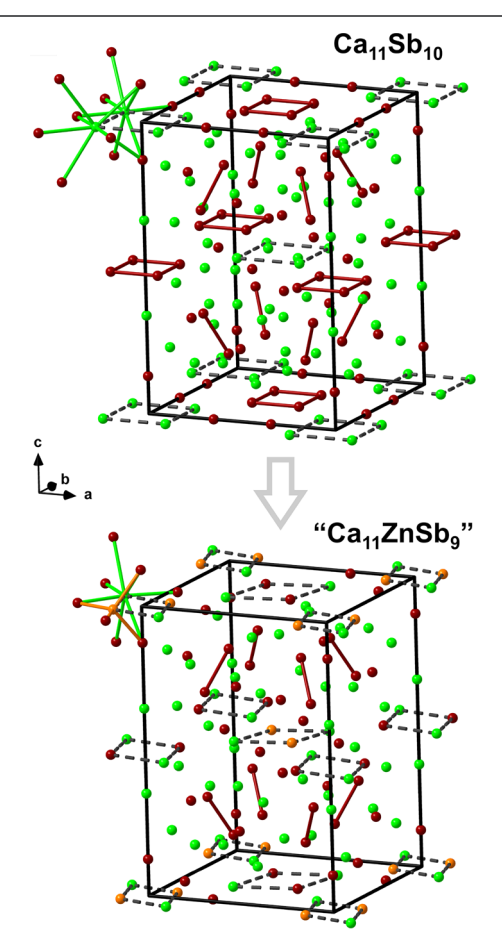


Figure 2. Crystal structure of $Ca_{11}Sb_{10}$ (top) and of the hypothetical derivative $Ca_{11}MSb_9$ with M = Zn (bottom). Covalent Sb–Sb bonding is shown with solid brown lines. Atomic rings that undergo changes upon the hypothetical transformation $Ca_{11}Sb_{10} \rightarrow Ca_{11}MSb_9$ are highlighted. Local coordination environment of selected metal atoms is emphasized. The unit cells are outlined in black. Ca, Zn, and Sb atoms are shown in green, orange, and brown, respectively.

anionic substructure of $Ca_{11}Sb_{10}$ can be viewed as consisting of isolated $[Sb_4]^{4-}$ square rings composed of Sb atoms in the Wyckoff sites 8h, $[Sb_2]^{4-}$ dumbbells built up of Sb(16m) atoms, and Sb^{3-} anions in the positions 8i, 4e, and 4d. The Ca atoms are located in between these Sb units. A fraction of the Ca substructure composed of the Ca(8h) atoms can be formally regarded as consisting of Ca_4 squares packed in a distorted fcc motif, similar to the $[Sb_4]^{4-}$ moieties. Upon symmetry reduction to space group $P4_2/mnm$, occurring via a klassengleiche transition with preservation of the unit cell, each 8h site splits into one 4f and one 4g site, while the 16m site splits into two 8j positions.

The multiplicities of other sites remain the same. A schematic representation of this transformation within the Bärnighausen tree formalism ⁷⁷ is given in Figure S3. By performing a hypothetical "chemical coloring" according to the scheme: $Sb(8h) \rightarrow Ca(4f) + Sb(4g)$ and $Ca(8h) \rightarrow Zn(4f) + Ca(4g)$ while keeping the chemical types of other sites as in the original structure, we arrive at the composition $Ca_{11}ZnSb_9$. The square Sb_4 and Ca_4 fragments in the original $Ca_{11}Sb_{10}$ structure transform into heteroatomic rhombi CaSbCaSb and

CaZnCaZn, respectively. Their shape is not imposed by a fourfold axis of rotation anymore. As suggested by the crystal structure refinements, the degree of distortion from a perfect square is driven by the need for optimization of the chemical bonding within such fragments. For instance, the CaZnCaZn rhombi adopt a favorable shape for realization of short covalent Zn—Sb contacts, which additionally results in the typical tetrahedral coordination of the Zn atoms by Sb atoms, while the Ca atoms remain sevenfold coordinated.

Note that the resulting hypothetical $Ca_{11}ZnSb_9$ structure is not related to the existing family of "11-1-9" Zintl pnictides, adopting the orthorhombic $Ca_{11}InSb_9$ structure type. ^{78–82} Instead, $Ca_{11}ZnSb_9$ is akin to the $Ca_{10}LiMgSb_9$ structure (Figure 2, bottom) where the Li position is taken by Ca, and Zn is assigned to the Mg position. ⁸³ A simple electron counting for $Ca_{11}MSb_9$ with M=Zn or Mn indicates that these compositions have an excess of one electron per formula unit according to the notation $(Ca^{2+})_{11}$ $(M^{2+})([Sb_2]^{4-})_2(Sb^{3-})_5$ (e⁻). Here, we assume oxidation state 2+ for both Zn and Mn. Following the same argumentation, the $Ca_{11}MSb_9$ compositions with M=Ga or In, which are trivalent, display an excess of two electrons per formula unit. In many intermetallic structures, the charge balance is restored via crystallographic disorder, which turns out to be the case here as well.

As already alluded to, the idealized Ca₁₁ZnSb₉ model, derived above, is an approximant and first step toward the understanding of the actual crystal structure. The generic formula Ca₁₀ZnSb₉ used throughout the paper is also only a simplified version of Ca_{10+x+y}Zn_{1-y}Sb₉ ($x\approx 0.2, y\approx 0.3$), somewhat deviating from it due to the excessive occupational and positional disorder (Figure 3a). In the course of the refinement, the position of the Zn atoms could be modeled as split into two distinct sites with a short distance of 1.01 Å between them, clearly signaling that they cannot be both occupied at the same time.

The Sb3 atom, located in the close vicinity of this split site, was also found to be affected by small but detectable splitting. From the analysis of the interatomic distances, the two positions resulting from the splitting of the Zn site were treated as Zn (labeled Zn1) and Ca (Ca4), while the Sb3 site was split into Sb3A and Sb3B. Free refinement of the occupancies with constrained atomic displacement parameters revealed that whenever the Zn1 site is occupied, it is tetrahedrally coordinated by two Sb5 atoms, showing full occupation and located at a distance of 2.79 Å from Zn1, and two Sb3B sites, located at a distance of 2.75 Å (Table 4). These values are in good agreement with bonding Zn–Sb contacts in other structures hosting ZnSb4 tetrahedra. 53,55,84–87

When the Ca4 position is filled, the Sb3 atoms have to move away to accommodate the larger Ca atom, which corresponds to the occupation of the Sb3A site, with the Ca4–Sb3A distance of 2.94 Å. Furthermore, the occupation of the Ca4 site was found to correlate with the splitting of another Sb position, Sb2 (Sb2 \rightarrow Sb2A + Sb2B): When present, Ca "pulls" the Sb2 atoms closer to complete its octahedral environment. The corresponding Ca4–Sb2A distance measures 3.66 Å (the complementary Sb2B site resides 3.97 Å away from Ca4, which is above the typical values for Ca–Sb bonding contacts $^{87-92}$). Finally, the location of the Ca4 site close to another Ca position, Ca5, and large atomic displacement parameters of the latter pointed toward underoccupation of Ca5, which prevents Ca4 and Ca5 to be located in the same volume of space simultaneously

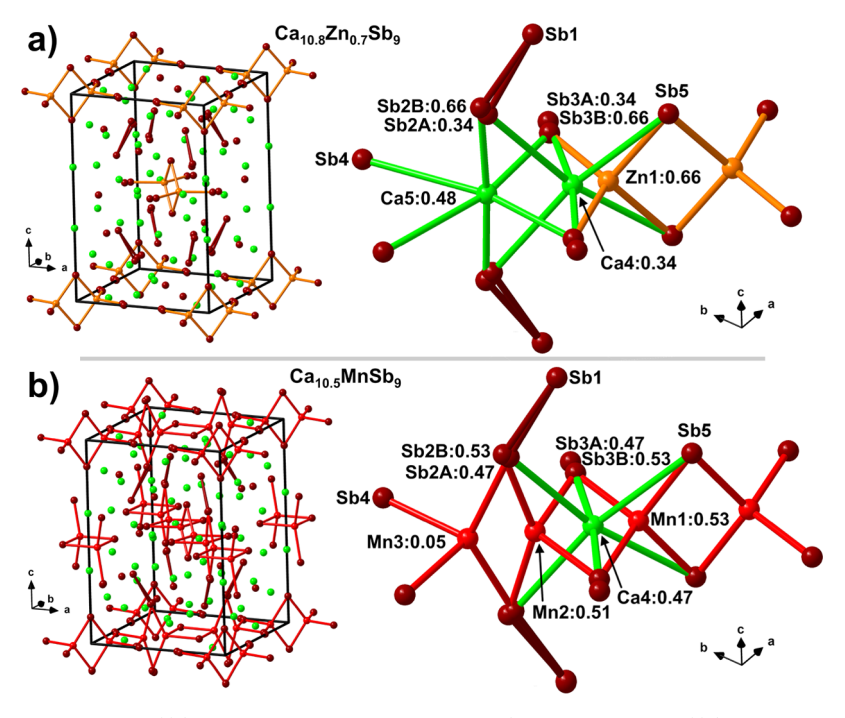


Figure 3. Crystal structures of $Ca_{10}ZnSb_9$ ((a), refined formula $Ca_{\sim 10.8}Zn_{\sim 0.7}Sb_9$) and $Ca_{10}MnSb_9$ ((b), refined formula $Ca_{\sim 10.5}Mn_{\sim 1}Sb_9$), and close-up view of the disordered parts of these structures. The occupancies of partially filled sites are indicated. Ca, Zn, Mn, and Sb atoms are depicted in green, orange, red, and brown, respectively. The unit cells are outlined in black.

Table 4. Selected Interatomic Distances (Å) in Ca₁₀ZnSb₉

	atoms	distance		atoms	distance
Ca1	—Sb6	3.144(2)	Ca4	—Zn1	1.01(1) ^a
	—Sb5	3.152(2)		—Ca5	$2.41(2)^a$
	—Sb2B	3.367(3)		$-Sb3B \times 2$	$2.438(3)^a$
	—Sb1	3.381(2)		$-Sb3A \times 2$	2.944(4)
	—Sb3B	3.386(2)		$-Sb5 \times 2$	3.51(1)
	—Sb1	3.434(2)		$-Sb2A \times 2$	3.66(1)
	—Sb3A	3.480(2)		$-Sb2B \times 2$	3.970(8)
	—Sb2A	3.53(1)	Ca5	$-Sb2A \times 2$	2.825(8)
	—Sb2A	3.608(6)		$-Sb2B \times 2$	3.080(4)
	—Sb2B	3.660(5)		$-Sb3B \times 2$	3.202(5)
Ca2	—Sb3A	3.071(4)		$-Sb3A \times 2$	3.625(7)
	—Sb1	3.111(2)		$-Sb4 \times 2$	3.836(5)
	—Sb6	3.166(2)	Ca6	$-Sb2B \times 2$	3.153(6)
	—Sb3A	3.182(4)		$-Sb4 \times 2$	3.298(3)
	—Sb2A	3.190(4)		$-Sb2A \times 2$	3.30(1)
	—Sb3B	3.201(2)		$-Sb1 \times 2$	3.7810(9)
	—Sb2B	3.254(2)		—Sb5	3.919(4)
	—Sb4	3.352(2)	Zn1	$-Sb3B \times 2$	2.753(3)
	—Sb3B	3.500(3)		$-Sb5 \times 2$	2.788(2)
Ca3	$-Sb3A \times 2$	3.031(4)		$-Sb3A \times 2$	3.200(4)
	$-Sb3B \times 2$	3.107(2)	Sb1	—Sb2B	2.862(5)
	—Sb4	3.323(3)		—Sb2A	3.00(1)
	$-Sb1 \times 2$	3.556(2)	Sb2A	—Sb2B	$0.314(9)^a$
	$-Sb5 \times 2$	3.646(2)	Sb3A	—Sb3B	$0.514(3)^a$
acı .	10 . 1 .				

"Short distances between the partially occupied sites with total occupancy ≤ 1 .

The total occupancy of Ca4 and Zn1 was found to be 100% within a few standard deviations and was fixed at this value at the later stages of the refinements. In addition, following the crystallographic reasoning given above, the occupancies were set to be equal within the pairs Zn1/Sb3B, Ca4/Sb3A, and Ca4/Sb2A, respectively (the occupation of the Sb2B site was

refined as complementary to that of Sb2A after refinements were run with unconstrained occupancies). The occupation of Ca5 was allowed to vary freely. The refined composition came out as Ca_{10.82(2)}Zn_{0.66(1)}Sb₉. Removing the occupancy constraints had virtually no effect on the refined formula. Since the crystallographic disorder in this case does not affect the formal charges, the electron accounting can be written as $(Ca^{2+})_{10.82(2)}(Zn^{2+})_{0.66(1)}([Sb_2]^{4-})_2(Sb^{3-})_5(h^+)_{0.04(6)}$, where h^+ stands for an electron-hole. The presented formula shows that the composition can be considered as charge-balanced within the error of the refinement. For the $Ca_{10+x+y}Zn_{1-y}Sb_9$ structures with M = Ga and In, similar crystallographic analysis yielded a very similar interplay between occupational and positional disorder and resulted in compositions approximately described by the formula $Ca_{10.9}M_{0.4}Sb_9$ (M = Ga, In). Here again, the electron balance appears to be achieved: $(Ca^{2+})_{10.9}(M^{3+})_{0.4}([Sb_2]^{4-})_2(Sb^{3-})_5.$

The disorder in $Ca_{10+x+y}Mn_{1-y}Sb_9$ displayed a somewhat different occupation pattern in comparison with the Zn representative (Figure 3b). Similar to Ca₁₀ZnSb₉, a splitting of the Mn site into a Mn (Mn1) and a Ca (Ca4) position was observed, accompanied by positional disorder of the surrounding Sb2 and Sb3 sites (Sb2 → Sb2A + Sb2B; Sb3 → Sb3A + Sb3B). However, attempts to refine the occupancy of the Ca5 site (as labeled in Ca10ZnSb9) led to a total occupancy of Ca4 and Ca5 of around 120%, which is impossible due to the unphysically short distance of 1.63 Å between the two sites, suggesting that only one of them can be filled at a time. In addition, the coordination environment of Ca5 appeared to be highly distorted. All these issues were remedied by treating the Ca5 position as Mn (labeled Mn2). Unlike the octahedrally coordinated Ca5 in Ca10ZnSb9, Mn2 adopts a tetrahedral environment of Sb atoms.

Close inspection of the difference Fourier map revealed the presence of yet another Mn position, Mn3, situated close to

Mn2 and displaying an almost negligible occupancy of about 5%. This position is also tetrahedrally coordinated by the neighboring Sb sites. In the final stages, the occupancies of Mn2 and Mn3 were freely refined, while their anisotropic displacement parameters were kept equal.

The Mn-Sb bonds involving Mn1 and Mn2 fall in the range 2.70-2.98 Å (Table 5), in line with the reported values in

Table 5. Selected Interatomic Distances in Ca₁₀MnSb₉

	atoms	distance		atoms	distance
Ca1	—Sb6	3.142(2)	Ca5	$-Sb2B \times 2$	3.18(3)
	—Sb5	3.157(2)		$-Sb4 \times 2$	3.257(3)
	—Sb3B	3.336(2)		$-Sb2A \times 2$	3.32(3)
	—Sb1	3.369(2)		$-Sb1 \times 2$	3.7832(9)
	—Sb2B	3.41(2)		—Sb5	3.872(4)
	—Sb1	3.440(2)	Mn1	$-Sb5 \times 2$	2.700(3)
	—Sb3A	3.451(2)		$-Sb3B \times 2$	2.816(4)
	—Sb2A	3.55(2)		-Mn2	2.909(6)
	—Sb2A	3.62(3)		-Mn1	3.112(9)
	—Sb2B	3.74(2)		$-Sb3A \times 2$	3.307(5)
Ca2	—Sb3A	3.094(3)	Mn2	-Mn3	$1.89(5)^a$
	—Sb1	3.147(2)		$-Sb2A \times 2$	2.83(3)
	—Sb3A	3.151(3)		$-Sb3B \times 2$	2.836(4)
	—Sb6	3.162(2)		$-Sb2B \times 2$	2.97(3)
	—Sb2A	3.16(1)		$-Sb3A \times 2$	3.265(4)
	—Sb2B	3.18(1)	Mn3	$-Sb2A\times 2$	3.01(4)
	—Sb3B	3.250(3)		$-Sb4 \times 2$	3.03(3)
	—Sb4	3.329(2)		$-Sb2B \times 2$	3.05(3)
	—Sb3B	3.530(3)	Sb1	—Sb2B	2.98(3)
Ca3	$-Sb3B \times 2$	3.046(3)		—Sb2A	3.00(3)
	$-Sb3A \times 2$	3.059(4)	Sb2A	—Sb2B	$0.19(3)^a$
	—Sb4	3.216(3)	Sb3A	—Sb3B	$0.528(3)^a$
	$-Sb1 \times 2$	3.514(2)			
	$-Sb5 \times 2$	3.723(2)			
Ca4	-Mn1	$1.278(8)^a$			
	-Mn2	$1.631(8)^a$			
	$-Sb3B \times 2$	$2.428(3)^a$			
	$-Sb3A \times 2$	2.955(3)			
	$-Sb2A\times 2$	3.58(3)			
	$-Sb5 \times 2$	3.592(6)			
	$-Sb2B\times 2$	3.77(2)			
		_		_	

"Short distances between the partially occupied sites with total occupancy ≤ 1 .

other structures with MnSb₄ tetrahedra. $^{44,47,88,92-97}$ The longest Mn—Sb contacts (2 × 3.01 Å and 2 × 3.04 Å) are observed around the Mn3 site. Their lengths might be overestimated due to some unresolved splitting of the Sb atoms in the Mn3 coordination sphere. Nevertheless, similar long Mn—Sb bonds were reported in some Zintl compounds with a distorted tetrahedral environment of Mn, e.g., $Sr_{21}Mn_4Sb_{18}^{98}$ and $Ca_{9-x}RE_xMn_4Sb_9$ (RE= rare-earth metal). 47

The final refined composition of the Mn member is $Ca_{10.48(1)}Mn_{1.09(2)}Sb_9$, which for simplicity has been approximated to $Ca_{10}MnSb_9$ throughout the text. Although the structures of the Zn and Mn members appear to slightly differ from each other, assignment of Mn^{2+} shows that it also conforms to the perfect electron count expected for a Zintl phase (within a few standard uncertainties): $(Ca^{2+})_{10.48(1)}(Mn^{2+})_{1.09(2)}([Sb_2]^{4-})_2(Sb^{3-})_5(e^-)_{0.14(6)}$. A possible reason for the realization of subtly different crystallographic

disorder in $Ca_{10}MnSb_9$ can be rooted in a strong magnetic exchange within the Mn substructure resulting in the formation of some extended units, such as broken chains of edge-sharing MnSb₄ tetrahedra. Magnetic interactions should always be considered when analyzing structure-stabilizing factors in crystalline materials. Our magnetic measurements confirm strong magnetic coupling between the Mn species in $Ca_{10}MnSb_9$ even well above room temperature (see below). A detailed representation of the crystallographic disorder, along with interatomic distances in $Ca_{10}MSb_9$ with M=Zn and Mn is given in Figure S4.

From the provided description, it can be concluded that, regardless of the nature of the metal M, the overall crystal structure of $Ca_{10+x+y}M_{1-y}Sb_9$ represents a highly disordered variant of $Ca_{10}LiMgSb_9$, so where the crystallographic disorder serves as a means to maintain an optimal valence electron count and keep the overall system charge-balanced. Materials that crystallize in the Ca₁₀LiMgSb₉ structure include, besides the prototype, Ca₁₀Mg₂Sb₉ and Ca_{10.62}Li_{1.38}Sb₉. 83 Although the latter compound has been suggested to display occupational disorder, the published description does not indicate that split positions similar to the ones described above have been considered in the refinement. However, based on the largest peak of the residual electron density, which is as high as 8.9 e-Å⁻³, we may speculate that some additional, unaccounted disorder ought to be present there as well. Whether this disorder is similar or different to what was described in the preceding paragraphs should be a matter of further studies.

The compositions of the Ca₁₀MSb₉ crystals determined in the course of the crystal structure refinements and EDX analysis were found to be consistent with each other within the error of the method (Table 1). It is important to note, however, that neither SCXRD nor EDX can provide highenough accuracy for uncovering compositional variations relevant for electronic transport properties. Indeed, if we consider the refined composition of the Zn representative, $(Ca^{2+})_{10.82(2)}(Zn^{2+})_{0.66(1)}([Sb_2]^{4-})_2(Sb^{3-})_5(h^+)_{0.04(6)}$, the number of holes can vary between 0 and 0.1 per formula unit within one standard-uncertainty interval. These values transform to hole concentrations of $0-10^{20}$ cm⁻³. While the lower limit corresponds to an intrinsic semiconductor, the upper limit resembles charge carrier concentrations in doped Zintl phases with good thermoelectric performance. Therefore, even though our refinements suggest charge-balanced compositions for the studied compounds, small self-doping due to deviations from the perfect Zintl count is possible and can drastically affect transport properties.

Lastly, since the structures of $Ca_{10}MSb_9$ (M = Ga, In, Mn, and Zn) are heavily affected by disorder, a natural question to ask is whether the discussed compounds exist in any appreciable homogeneity ranges. To check for possible compositional variations, we prepared additional $Ca_{10+x+\nu}Zn_{1-\nu}Sb_9$ samples with varying Ca/Zn ratios. The reactions were done in welded Nb tubes, as described in the Experimental Section. The results of the SCXRD analysis indicate a very narrow homogeneity range, between about Ca_{10.8}Zn_{0.7}Sb₉ and Ca_{10.9}Zn_{0.6}Sb₉. Note that the increase in the Zn content is associated with a decrease in the Ca amount so that the ideal Zintl count is retained. Crystallographic data, atomic coordinates, and selected interatomic distances for the second crystal, which was selected from a reaction batch that was nominally richer in Ca, are given in Tables S5-S7. From a crystallographic perspective, the increase of the Ca/Zn ratio

results in a slight expansion of the unit cell (see Tables 1 and S5). This is due to the larger atomic size of Ca vs Zn, but the bonding distances are not affected significantly, which means that the chemical bonding pattern is preserved. In general, since the covalent M–Sb bonds in $Ca_{10}MSb_9$ lie predominantly in the ab plane or at an angle to this plane, the tetragonal cell experiences the strongest size changes in the ab plane upon replacing the metal M or changing the occupation of its position. Concomitantly, the expansion of the cell in the ab plane is accompanied by shrinking along the c direction and vice versa, which maintains the optimal packing density.

Although we did not perform a systematic analysis of the homogeneity ranges in other representatives of the Ca₁₀MSb₉ family, the SCXRD data on crystals from different batches suggest only minor compositional variations for all of them.

3.3. Electronic Structure and Chemical Bonding. Owing to the fact that accurate modeling of the extensive disorder in Ca₁₀MSb₉ is quite challenging, we evaluated electronic properties of an idealized Ca₁₁ZnSb₉ adopting the Ca₁₀LiMgSb₉ structure (Figure 2, bottom). This hypothetical, disorder-free model is a reasonably close variant of the actual version of Ca_{10.8}Zn_{0.7}Sb₉ structure and was derived as follows: (i) the initial lattice parameters and the atomic coordinates were taken from the refinement of the single-crystal X-ray diffraction data (Table 2); (ii) the partially occupied sites Ca4, Sb2A, and Sb3A were removed; and (iii) the remaining atomic positions were treated as fully occupied. The as-derived structure was then fully relaxed. Although such an oversimplification cannot provide fine details of the electronic structure, it can give some valuable information about the chemical interactions in the real system in question.

The electronic density of states (DOS) for the Ca₁₁ZnSb₉ model is shown in Figure 4a. In line with the expected charge transfer from the atoms of the electropositive Ca to the Sb

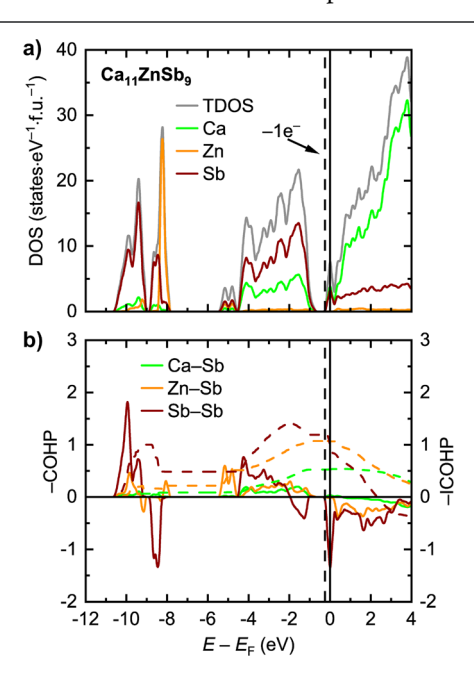


Figure 4. Total and projected electronic densities of state (DOSs) for the idealized $Ca_{11}ZnSb_9$ model (a) and crystal orbital Hamilton population curves (COHP) for averaged selected interactions (b). The vertical solid line marks the position of the Fermi level; the vertical dashed line indicates the expected position of the Fermi level after removal of one electron per formula unit.

atoms, the DOS is dominated by the occupied Sb states below the Fermi level ($E_{\rm F}$), whereas the empty Ca states are located predominantly above—an electronic pattern typical for pnictides containing alkaline earth metals. $^{5,37,101-103}$

The contribution of the Zn states in the vicinity of $E_{\rm F}$ is minor due to a relatively small fraction of Zn atoms in the unit cell, and these states are hybridized with the Sb(5p) states. A domain of highly localized occupied Zn(3d) states is located below $E - E_F = -8$ eV. The DOS at these energies is also characterized by several peaks with the Sb character, corresponding to the Sb lone pairs and electronic levels of the Sb₂ dumbbells. The Fermi level crosses a finite DOS situated just above an electronic bandgap with a size of about 0.5 eV. This value is comparable to the bandgap widths in the Zintl pnictides $Yb_{14}MSb_{11}$ with M = Mg, Al, and Mn, in the semiconducting regime. As discussed above, the Ca₁₁ZnSb₉ model shows an excess of one electron per formula unit: $(Ca^{2+})_{11}(Zn^{2+})([Sb_2]^{4-})_2(Sb^{3-})_5(e^-)$. Assuming that the rigid band approximation is applicable in this case, a removal of one electron from Ca₁₁ZnSb₉ would shift the Fermi level into the bandgap, thereby achieving a charge-balanced state, in accordance with the simple electron bookkeeping provided above. It is worthwhile to note that the DOS below the gap is rather steep, which is expected to yield high thermopower, S, beneficial for good thermoelectric performance. Inspection of the electronic band structure (Figure S5) indicates that the steep DOS results from alignment of the band edges and band degeneracy rather than the presence of any flat bands. The relatively high dispersion of the bands close to the gap opening is anticipated to yield small effective electron masses and hence high mobility, which is also essential for a good thermoelectric material.

To analyze how electron depletion accompanying restoration of the Zintl count affects the chemical bonding, we plotted the crystal orbital Hamilton population curves (COHP) for averaged selected interactions (Figure 4b). Although the Ca-Sb contacts dominate the structure in terms of their number, the average negative integrated COHP value per bond at $E_{\rm F}$ (-ICOHP) is relatively small, due to high ionicity of such bonds. Most of the available bonding Ca-Sb states are occupied below the opening of the bandgap in the electronic spectrum. Consequently, shifting the Fermi level into the gap would not affect the Ca-Sb bonding considerably. In contrast to the Ca-Sb contacts, the Zn-Sb and Sb-Sb interactions are strongly covalent. The Zn-Sb states have almost entirely bonding character below $E_{\rm F}$, whereas the electronic interactions in the Sb₂ dumbbells are hallmarked by the presence of bonding and antibonding states in a manner typical for this kind of structural units. $^{105-113}$ An important feature to highlight here is the location of the Fermi level within domains of antibonding states for the Zn-Sb and Sb-Sb bonds. Notice that the E_F is situated right at a peak with a pronounced antibonding character. The main implication of these electronic features is underoptimization of the Zn-Sb and Sb-Sb bonding. By shifting the Fermi level out of the antibonding region into the bandgap below, the interactions can be brought to their optimized values. The presented electronic behavior of the hypothetical Ca₁₁ZnSb₉ compound suggests that removal of excessive electrons is important for stabilization of the structure. The observed compositional (and associated positional) disorder in Ca_{10.8}Zn_{0.7}Sb₉ must originate therefore from the tendency of the system to restore its chargebalanced composition and stabilize the chemical bonding by

this means. We believe that the same argumentation is valid for the $Ca_{10+x+y}M_{1-y}Sb_9$ compositions with other M as well. It would be interesting to check if substitution of a metal with oxidation state +1 for M in $Ca_{10+x+y}M_{1-y}Sb_9$ is possible and whether it could lead to a disorder-free $Ca_{11}MSb_9$ structure satisfying the Zintl partitioning $(Ca^{2+})_{11}(M^{1+})$ - $([Sb_2]^{4-})_2(Sb^{3-})_5$. Possible candidate metals for such future studies could be the coinage elements of group 11 (Cu, Ag, Au) or Li. As was mentioned above, the composition $Ca_{10.62}Li_{1.38}Sb_9$ has already been reported to crystallize in the targeted structure. However, the published $Ca_{10.62}Li_{1.38}Sb_9$ structural data have to be used with caution due to the significant residual electron density. This points toward potential inadequacy of the model (e.g., unresolved disorder) and calls for additional structural studies.

3.4. Electrical Resistivity. Low-temperature electrical resistivity measurements on the single crystals of $Ca_{10}MSb_9$ (M = Ga, In, Mn) indicate consistency with extrinsic semiconducting behavior (Figure 5). In the case of $Ca_{10}GaSb_9$,

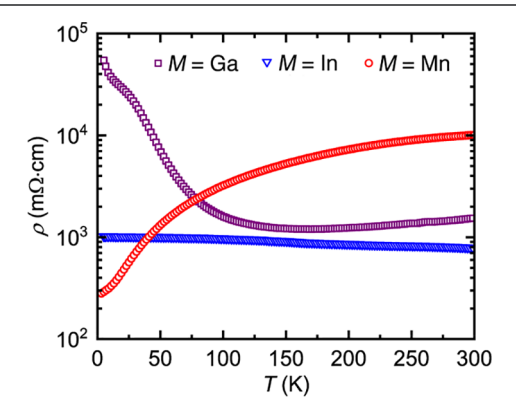


Figure 5. Temperature-dependence of electrical resistivity for single crystals of $Ca_{10}MSb_9$ (M = Ga, In, Mn).

the resistivity $\rho(T)$ can be seen to decrease upon heating up to about 170 K. After that, a weak gradual increase is observed up to a room temperature value of 2 Ω ·cm. The electrical resistivity of $Ca_{10}InSb_9$ is weakly temperature-dependent and stays around 1 Ω ·cm in the whole measured temperature region. Finally, the single crystals of $Ca_{10}MnSb_9$ demonstrate a degenerate semiconducting behavior with a continuous increase of electrical resistivity from 0.3 Ω ·cm at 5 K to 10 Ω ·cm at room temperature.

Several measured $Ca_{10}MnSb_9$ crystals showed well-reproducible $\rho(T)$ curves. In contrast, for different crystals with M=Ga or In, even if extracted from the same batch, there were small variations in the temperature-dependence of the electrical resistivity. The latter could be attributed to varying self-doping levels. Since the crystals grow under constantly changing conditions (temperature, composition of the melt), different crystals from the same reaction or even different parts of a crystal may have inherent inhomogeneities, which result in irreproducible transport data. However, the absolute values of $\rho(T)$ at room temperature for those crystals were always on the order of 1 Ω ·cm, which is about 2–3 orders of magnitude higher than the corresponding values in benchmark thermoelectric materials, such as PbTe, Yb₁₄MnSb₁₁, and their derivatives.

3.5. Magnetization. Magnetization measurements on single crystals of the Mn-bearing member, conducted below

room temperature, reveal a weakly temperature-dependent response. The small upturn at low temperatures is likely due to a paramagnetic impurity phase (Figure S6). The deviation of the magnetic susceptibility curve from a typical Curie—Weiss behavior, together with the non-negligible field-dependence, pointed toward magnetic ordering above room temperature.

High-temperature magnetization measurements up to 950 K uncovered two magnetic transitions (Figure 6). Upon cooling,

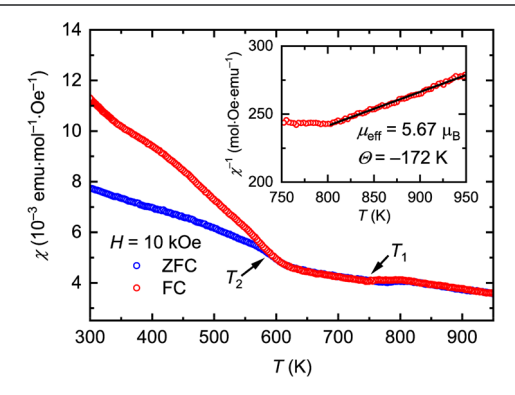


Figure 6. Temperature-dependence of magnetic susceptibility for a $Ca_{10}MnSb_9$ single crystal in the range T=300-950 K. Zero-field-cooled (ZFC) and field-cooled (FC) measurements are shown in blue and red, respectively. Inset: linear fit (black curve) of the inverse susceptibility versus temperature (red open circles).

the sample first undergoes an antiferromagnetic-like transition at T_1 = 780 K, followed by a second transition at T_2 = 580 K. The transition at T_2 is accompanied by development of a weak uncompensated magnetic moment. It is worth noting that the value of T_2 is close to the Curie temperature of the binary manganese antimonide MnSb (T_C = 587 K), the which could have formed on the surface of the specimen upon contact with the water-based Zircar cement used for the sample immobilization. The parasitic ferromagnetism of a MnSb impurity could explain the observed net magnetization of the sample below 580 K. PXRD analysis of the crystal after the measurement did not indicate any deterioration in the bulk of the sample.

Fitting of the inverse susceptibility versus temperature in the paramagnetic region above 780 K yielded a magnetic moment of $5.67~\mu_{\rm B}$, which is close to the expected spin-only value for a high-spin Mn²⁺ ($5.92~\mu_{\rm B}$). The apparent reduction of the moment can be an artifact associated with the noise in the measured data at high temperatures, inaccuracy of the crystal weighing, or from a somewhat lower Mn content in the measured crystal (corresponding to a shortage of about 8% Mn in comparison with the refined formula ${\rm Ca_{10.48(1)}Mn_{1.09(2)}Sb_9}$). Thus, the magnetization measurements confirm the presence of Mn²⁺ in the measured sample and provide another substantiation of the refined chemical composition.

We would like to conclude the discussion of the magnetism with a note that the observed transition temperature of 780 K in $\text{Ca}_{10}\text{MnSb}_9$ is unexpectedly high for a compound exhibiting crystallographic disorder of the magnetic species in the structure. This discovery deserves further investigations, and it can be envisioned that the optimized crystal growth procedure described in the Experimental Section will afford samples suitable for detailed neutron scattering studies.

3.6. High-Temperature Transport Properties. There is reasonable agreement in the room temperature resistivity

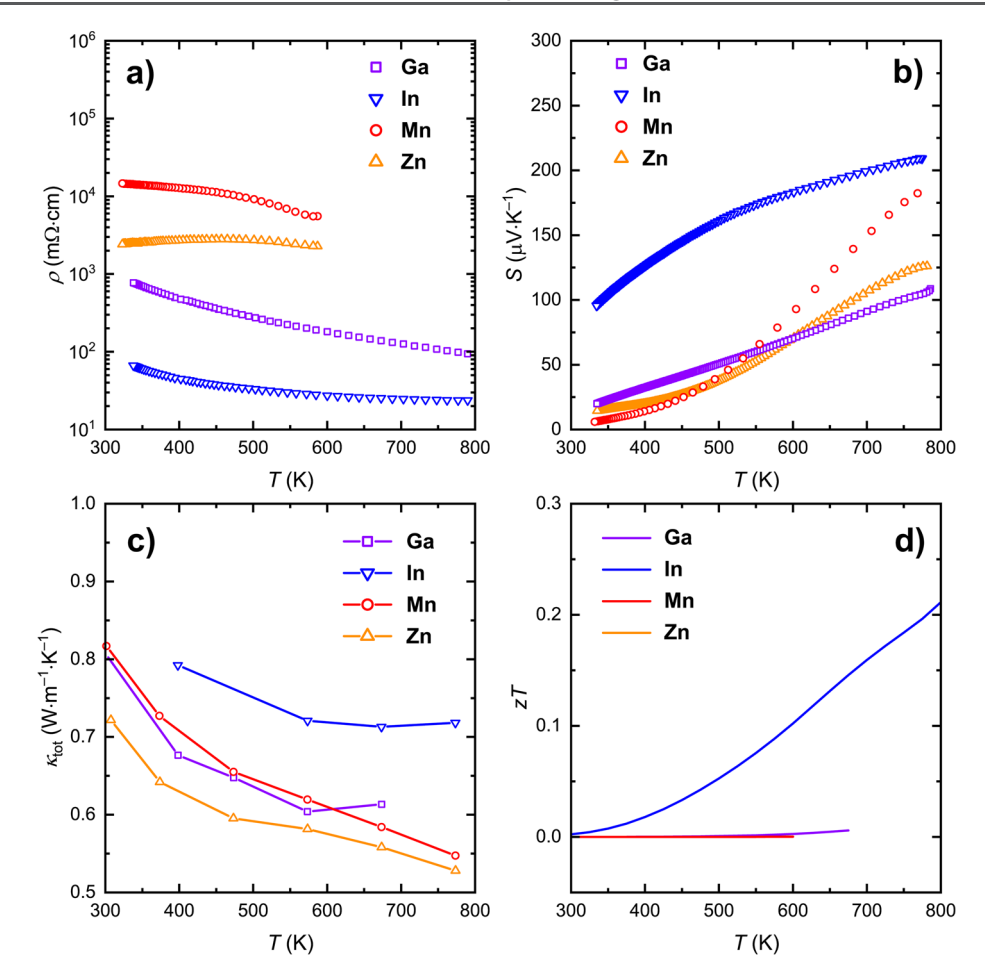


Figure 7. High-temperature thermoelectric properties of $Ca_{10}MSb_9$ (M = Ga, In, Mn, Zn): Temperature-dependence of electrical resistivity (a), Seebeck coefficient (b), thermal conductivity (c), and thermoelectric figure of merit, zT (d).

between the single crystals measured on the PPMS (Figure 5) and the polycrystalline pellets measured using the van der Pauw method (Figure 7a). In both sets of measurements, the M= In sample has the lowest resistivity, followed by M= Ga and M= Mn. Interestingly, the resistivity of the polycrystalline M= In sample at room temperature (0.07 $\Omega \cdot$ cm) is about an order of magnitude lower than the corresponding value for the single crystal. This is likely related to small differences in composition (and thus self-doping) between the flux-grown crystals and polycrystalline materials. The synthesis conditions have a large impact on the chemical potential during growth, which in turn impacts defect formation energies. It is reasonable to expect differences in defect concentrations of an order of magnitude or more, leading to corresponding changes in the charge concentration.

For M = Mn, the electrical resistivity has the highest value among the measured samples. For M = Zn, the electrical resistivity stays between the values for M = Ga and M = Mn in the whole measured temperature region. The gradual decrease in resistivity at high temperatures suggests that the samples are semiconductors. The temperature-dependence of the electrical resistivity deviates from exponential behavior even at the highest measured temperature, indicating that the intrinsic regime is not achieved, which hindered determination of the bandgaps from the resistivity data.

However, the metal-like behavior of the temperaturedependent Seebeck coefficient (i.e., close to zero magnitude at room temperature and monotonic increase with temperature) presents a more complicated story (see Figure 7b). The low room-temperature Seebeck coefficients in samples with M=Mn, Zn, and Ga when compared to their very large resistivities at their respective temperatures suggests the presence of multiple carriers, i.e., bipolar conduction, resulting from competition of holes as the majority carrier, and electrons as the minority carrier. Bipolar transport can result from either a high *concentration* of minority carriers (due to a small band gap) or from a high *mobility* of secondary carriers due to differences in the band mass or scattering of the two carrier types.

The compound with M= In exhibited the largest Seebeck coefficient despite being the least resistive sample, suggesting that this sample is the only one to have holes as the dominant carrier type across the entire temperature range. Using the maximum observed Seebeck value, we can estimate a *minimum* bound for the band gap of $E_{\rm g}=0.32$ eV using the Goldsmid–Sharp approximation. These results point to the importance of doping to reach a single-carrier regime to gain insight into electronic transport in this class of material. It is worth noting that the structurally related binary antimonides $AE_{11}Sb_{10}$ (AE=Ca, Yb) also display bipolar conduction. However, in these compounds, the majority and minority charge carriers almost perfectly compensate each other, leading to low values of the Seebeck coefficient.

The temperature-dependent thermal conductivity seen in Figure 7c is exceptionally low for all samples and comparable to materials such as Yb₁₄MnSb₁₁, ¹³ Yb₉Mn_{4.2}Sb₉, ⁴⁵ Sr₃GaSb₃, ³²

and n-type Mg_3Sb_2 . This exceedingly low thermal conductivity is consistent with the large number of atoms per unit cell and considerable disorder. The rather low electronic conductivities of the samples indicate that the total thermal conductivities, κ_{tov} are reasonable representatives of the lattice contribution, κ_L . The M = In sample is expected to have the largest electronic contribution to thermal conductivity, κ_{ev} likely leading to the slightly higher total thermal conductivity. However, even in that case, κ_{e} is quite small.

The figure of merit, zT, for the measured samples is shown in Figure 7d. While the Ca₁₀MSb₉ samples with M=Zn and Mn display negligibly low zT values of about 10^{-4} up to T=600 K, the Ga representative has a zT of 0.01 at T=700 K. The highest value of 0.2 is observed for M=In at T=800 K. Note that the value of zT at room temperature for the zT0 is missing at room temperature. Considering that the carrier concentration in these materials was not optimized in any way, the observed zT1 values are quite promising, particularly for the In member.

It can be expected that with proper doping, a single-carrier regime will be achieved, which will improve the electrical conductivity and increase the thermopower. Since holes appear to be the major charge carriers, hole doping should be used to eliminate bipolar conduction. This can be likely accomplished by chemical substitutions in the M sites of the crystal structure or by replacing Ca with a monovalent metal, e.g., an alkali metal. The existence of the structurally related Li-bearing phases $Ca_{10}LiMgSb_9$ and $Ca_{10.62}Li_{1.38}Sb_9$ suggests that the latter kind of doping may be possible. In addition, a transition from antimonides to bismuthides may be an efficient way to increase the electrical conductivity and probably reduce the thermal conductivity even further, owing to the high atomic mass of Bi.

4. CONCLUSIONS

In this contribution, we presented a new family of Zintl phases, exemplified by the antimonides with the approximate composition $Ca_{10}MSb_9$ (M = Ga, In, Mn, Zn). The studied compounds adopt a complex crystal structure with extensive occupational and positional disorder, which lends these materials efficient phonon scattering, reflected in their extremely low thermal conductivity. Furthermore, the development of the crystallographic disorder is accompanied by attainment of perfect charge balance and leads to semiconducting behavior with high thermopower. The latter likely originates from a steep density of electronic states in the vicinity of the Fermi level, as indicated by our first-principle calculations on an idealized structural model. The presence of competing electrons and holes as charge carriers in these new antimonides results in relatively poor electrical conductivity. However, even in the bipolar conduction regime, a thermoelectric figure of merit, zT, as high as 0.2 can be achieved for the In member. We believe that with proper doping, the thermoelectric performance can be further improved, especially if the doped materials enter the single-carrier conduction regime. In addition, our preliminary data suggest the existence of other members of this structural family, 120 which opens up possibilities for further studies.

ASSOCIATED CONTENT

Supporting Information

The Supporting Information is available free of charge at https://pubs.acs.org/doi/10.1021/acs.chemmater.0c04940.

X-ray data (CIF)

Tables with crystal structure data, PXRD patterns, representation of the group—subgroup relationship, detailed depiction of the crystallographic disorder, and low-temperature magnetization data (PDF)

AUTHOR INFORMATION

Corresponding Author

Svilen Bobev — Department of Chemistry and Biochemistry, University of Delaware, Newark, Delaware 19716, United States; orcid.org/0000-0002-0780-4787; Email: bobev@udel.edu

Authors

Alexander Ovchinnikov — Department of Chemistry and Biochemistry, University of Delaware, Newark, Delaware 19716, United States; Department of Materials and Environmental Chemistry, Stockholm University, 10691 Stockholm, Sweden; Occid.org/0000-0002-0537-4234

Sevan Chanakian – Department of Chemical Engineering and Materials Science, Michigan State University, East Lansing, Michigan 48824, United States; orcid.org/0000-0003-0482-4069

Alexandra Zevalkink — Department of Chemical Engineering and Materials Science, Michigan State University, East Lansing, Michigan 48824, United States; orcid.org/0000-0002-4672-7438

Complete contact information is available at: https://pubs.acs.org/10.1021/acs.chemmater.0c04940

Author Contributions

All authors have given approval to the final version of the manuscript.

Notes

The authors declare no competing financial interest.

ACKNOWLEDGMENTS

We thank Dr. Sviatoslav Baranets for the EDX analysis and for preliminary work on the structurally related bismuthides and Yb₁₀MnSb₉. This work was supported by the U.S. Department of Energy, Office of Science, Basic Energy Sciences, under Award No. DE-SC0008885. Synthesis-related tasks performed by S.C. and A.Z. were supported by the National Science Foundation (NSF) award number 1709158. SC's contributions are based upon work supported by the National Science Foundation Graduate Research Fellowship Program award number DGE-1848739. We would like to thank Dr. Sabah Bux and the Radioisotope Power Systems Program's Thermoelectric Technology Development group at the Jet Propulsion Laboratory (JPL) for allowing us to use their measurement facilities. Additionally, we would like to thank George Nakatsukasa and Gregory Gerig for their assistance in measuring the temperature-dependent thermal diffusivity and Seebeck coefficients, respectively.

REFERENCES

(1) Zeier, W. G.; Zevalkink, A.; Gibbs, Z. M.; Hautier, G.; Kanatzidis, M. G.; Snyder, G. J. Thinking Like a Chemist: Intuition in

- Thermoelectric Materials. Angew. Chem., Int. Ed. 2016, 55 (24), 6826–6841.
- (2) Zevalkink, A.; Smiadak, D. M.; Blackburn, J. L.; Ferguson, A. J.; Chabinyc, M. L.; Delaire, O.; Wang, J.; Kovnir, K.; Martin, J.; Schelhas, L. T.; Sparks, T. D.; Kang, S. D.; Dylla, M. T.; Snyder, G. J.; Ortiz, B. R.; Toberer, E. S. A Practical Field Guide to Thermoelectrics: Fundamentals, Synthesis, and Characterization. *Appl. Phys. Rev.* 2018, 5 (2), 021303.
- (3) Kauzlarich, S. M.; Brown, S. R.; Snyder, G. J. Zintl Phases for Thermoelectric Devices. *Dalton Trans.* **2007**, *0* (21), 2099–2107.
- (4) Toberer, E. S.; May, A. F.; Snyder, G. J. Zintl Chemistry for Designing High Efficiency Thermoelectric Materials. *Chem. Mater.* **2010**, 22 (3), 624–634.
- (5) Ovchinnikov, A.; Bobev, S. Zintl Phases with Group 15 Elements and the Transition Metals: A Brief Overview of Pnictides with Diverse and Complex Structures. *J. Solid State Chem.* **2019**, 270, 346–359.
- (6) Ovchinnikov, A.; Smetana, V.; Mudring, A.-V. Metallic Alloys at the Edge of Complexity: Structural Aspects, Chemical Bonding and Physical Properties. *J. Phys.: Condens. Matter* **2020**, 32 (24), 243002.
- (7) Kleinke, H. New Bulk Materials for Thermoelectric Power Generation: Clathrates and Complex Antimonides. *Chem. Mater.* **2010**, 22 (3), 604–611.
- (8) Dolyniuk, J.-A.; Owens-Baird, B.; Wang, J.; Zaikina, J. V.; Kovnir, K. Clathrate Thermoelectrics. *Mater. Sci. Eng., R* **2016**, *108*, 1–46.
- (9) Wang, J.; Wang, L.-L.; Kovnir, K. Phonon Glass Behavior beyond Traditional Cage Structures: Synthesis, Crystal and Electronic Structure, and Properties of KMg₄Sb₃. *J. Mater. Chem. A* **2018**, *6* (11), 4759–4767.
- (10) Owens-Baird, B.; Wang, J.; Wang, S. G.; Chen, Y.-S.; Lee, S.; Donadio, D.; Kovnir, K. III–V Clathrate Semiconductors with Outstanding Hole Mobility: $Cs_8In_{27}Sb_{19}$ and $A_8Ga_{27}Sb_{19}$ (A = Cs, Rb). J. Am. Chem. Soc. **2020**, 142 (4), 2031–2041.
- (11) Owens-Baird, B.; Yox, P.; Lee, S.; Carroll, X. B.; Grass Wang, S.; Chen, Y.-S.; Lebedev, O. I.; Kovnir, K. Chemically Driven Superstructural Ordering Leading to Giant Unit Cells in Unconventional Clathrates Cs₈Zn₁₈Sb₂₈ and Cs₈Cd₁₈Sb₂₈. *Chem. Sci.* **2020**, *11* (37), 10255–10264.
- (12) Brown, S. R.; Kauzlarich, S. M.; Gascoin, F.; Snyder, G. J. Yb₁₄MnSb₁₁: New High Efficiency Thermoelectric Material for Power Generation. *Chem. Mater.* **2006**, *18* (7), 1873–1877.
- (13) Toberer, E. S.; Cox, C. A.; Brown, S. R.; Ikeda, T.; May, A. F.; Kauzlarich, S. M.; Snyder, G. J. Traversing the Metal-Insulator Transition in a Zintl Phase: Rational Enhancement of Thermoelectric Efficiency in Yb₁₄Mn_{1-x}Al_xSb₁₁. Adv. Funct. Mater. **2008**, 18 (18), 2795–2800.
- (14) Brown, S. R.; Toberer, E. S.; Ikeda, T.; Cox, C. A.; Gascoin, F.; Kauzlarich, S. M.; Snyder, G. J. Improved Thermoelectric Performance in Yb₁₄Mn_{1-x}Zn_xSb₁₁ by the Reduction of Spin-Disorder Scattering. *Chem. Mater.* **2008**, *20* (10), 3412–3419.
- (15) Condron, C. L.; Kauzlarich, S. M.; Gascoin, F.; Snyder, G. J. Thermoelectric Properties and Microstructure of Mg₃Sb₂. J. Solid State Chem. **2006**, 179 (8), 2252–2257.
- (16) Zhang, J.; Song, L.; Pedersen, S. H.; Yin, H.; Hung, L. T.; Iversen, B. B. Discovery of High-Performance Low-Cost *n*-Type Mg₃Sb₂-Based Thermoelectric Materials with Multi-Valley Conduction Bands. *Nat. Commun.* **2017**, *8* (1), 13901.
- (17) Imasato, K.; Kang, S. D.; Ohno, S.; Snyder, G. J. Band Engineering in Mg₃Sb₂ by Alloying with Mg₃Bi₂ for Enhanced Thermoelectric Performance. *Mater. Horiz.* **2018**, 5 (1), 59–64.
- (18) Gascoin, F.; Ottensmann, S.; Stark, D.; Haïle, S. M.; Snyder, G. J. Zintl Phases as Thermoelectric Materials: Tuned Transport Properties of the Compounds Ca_xYb_{1-x}Zn₂Sb₂. *Adv. Funct. Mater.* **2005**, *15* (11), 1860–1864.
- (19) Wang, X.-J.; Tang, M.-B.; Zhao, J.-T.; Chen, H.-H.; Yang, X.-X. Thermoelectric Properties and Electronic Structure of Zintl Compound BaZn₂Sb₂. *Appl. Phys. Lett.* **2007**, *90* (23), 232107.
- (20) Zhang, H.; Zhao, J.-T.; Grin, Yu.; Wang, X.-J.; Tang, M.-B.; Man, Z.-Y.; Chen, H.-H.; Yang, X.-X. A New Type of Thermoelectric Material, EuZn₂Sb₂. *J. Chem. Phys.* **2008**, *129* (16), 164713.

- (21) Wang, X.-J.; Tang, M.-B.; Chen, H.-H.; Yang, X.-X.; Zhao, J.-T.; Burkhardt, U.; Grin, Yu. Synthesis and High Thermoelectric Efficiency of Zintl Phase YbCd_{2-x}Zn_xSb₂. *Appl. Phys. Lett.* **2009**, 94 (9), 092106.
- (22) Zhang, H.; Baitinger, M.; Tang, M.-B.; Man, Z.-Y.; Chen, H.-H.; Yang, X.-X.; Liu, Y.; Chen, L.; Grin, Yu.; Zhao, J.-T. Thermoelectric Properties of $Eu(Zn_{1-x}Cd_x)_2Sb_2$. Dalton Trans. **2010**, 39 (4), 1101–1104.
- (23) Cao, Q.-G.; Zhang, H.; Tang, M.-B.; Chen, H.-H.; Yang, X.-X.; Grin, Yu.; Zhao, J.-T. Zintl Phase Yb_{1-x}Ca_xCd₂Sb₂ with Tunable Thermoelectric Properties Induced by Cation Substitution. *J. Appl. Phys.* **2010**, *107* (5), 053714.
- (24) Zhang, H.; Fang, L.; Tang, M.-B.; Man, Z. Y.; Chen, H. H.; Yang, X. X.; Baitinger, M.; Grin, Yu.; Zhao, J.-T. Thermoelectric Properties of Yb_xEu_{1-x}Cd₂Sb₂. *J. Chem. Phys.* **2010**, *133* (19), 194701.
- (25) Zhang, H.; Tang, M.-B.; Schnelle, W.; Baitinger, M.; Man, Z.-Y.; Chen, H.-H.; Yang, X.-X.; Zhao, J.-T.; Grin, Yu. Thermoelectric Properties of Polycrystalline SrZn₂Sb₂ Prepared by Spark Plasma Sintering. *J. Electron. Mater.* **2010**, 39 (9), 1772–1776.
- (26) Toberer, E. S.; May, A. F.; Melot, B. C.; Flage-Larsen, E.; Snyder, G. J. Electronic Structure and Transport in Thermoelectric Compounds AZn_2Sb_2 (A = Sr, Ca, Yb, Eu). Dalton Trans. **2010**, 39 (4), 1046–1054.
- (27) Guo, K.; Cao, Q.-G.; Feng, X.-J.; Tang, M.-B.; Chen, H.-H.; Guo, X.; Chen, L.; Grin, Yu.; Zhao, J.-T. Enhanced Thermoelectric Figure of Merit of Zintl Phase YbCd_{2-x}Mn_xSb₂ by Chemical Substitution. *Eur. J. Inorg. Chem.* **2011**, 2011 (26), 4043–4048.
- (28) Zevalkink, A.; Zeier, W. G.; Cheng, E.; Snyder, J.; Fleurial, J.-P.; Bux, S. Nonstoichiometry in the Zintl Phase $Yb_{1-\delta}Zn_2Sb_2$ as a Route to Thermoelectric Optimization. *Chem. Mater.* **2014**, *26* (19), 5710–5717.
- (29) Pomrehn, G. S.; Zevalkink, A.; Zeier, W. G.; van de Walle, A.; Snyder, G. J. Defect-Controlled Electronic Properties in AZn_2Sb_2 Zintl Phases. *Angew. Chem., Int. Ed.* **2014**, *53* (13), 3422–3426.
- (30) Peng, W.; Chanakian, S.; Zevalkink, A. Crystal Chemistry and Thermoelectric Transport of Layered AM₂X₂ Compounds. *Inorg. Chem. Front.* **2018**, 5 (8), 1744–1759.
- (31) Zevalkink, A.; Toberer, E. S.; Zeier, W. G.; Flage-Larsen, E.; Snyder, G. J. Ca₃AlSb₃: An Inexpensive, Non-Toxic Thermoelectric Material for Waste Heat Recovery. *Energy Environ. Sci.* **2011**, *4* (2), 510–518.
- (32) Zevalkink, A.; Zeier, W. G.; Pomrehn, G.; Schechtel, E.; Tremel, W.; Snyder, G. J. Thermoelectric Properties of Sr₃GaSb₃ a Chain-Forming Zintl Compound. *Energy Environ. Sci.* **2012**, *5* (10), 9121–9128.
- (33) Zeier, W. G.; Zevalkink, A.; Schechtel, E.; Tremel, W.; Snyder, G. J. Thermoelectric Properties of Zn-Doped Ca₃AlSb₃. *J. Mater. Chem.* **2012**, 22 (19), 9826–9830.
- (34) Toberer, E. S.; Zevalkink, A.; Crisosto, N.; Snyder, G. J. The Zintl Compound $Ca_5Al_2Sb_6$ for Low-Cost Thermoelectric Power Generation. *Adv. Funct. Mater.* **2010**, 20 (24), 4375–4380.
- (35) Zevalkink, A.; Toberer, E. S.; Bleith, T.; Flage-Larsen, E.; Snyder, G. J. Improved Carrier Concentration Control in Zn-Doped Ca₅Al₂Sb₆. *J. Appl. Phys.* **2011**, *110* (1), 013721.
- (36) Zevalkink, A.; Pomrehn, G. S.; Johnson, S.; Swallow, J.; Gibbs, Z. M.; Snyder, G. J. Influence of the Triel Elements (M = Al, Ga, In) on the Transport Properties of $Ca_5M_2Sb_6$ Zintl Compounds. *Chem. Mater.* **2012**, 24 (11), 2091–2098.
- (37) Zevalkink, A.; Chanakian, S.; Aydemir, U.; Ormeci, A.; Pomrehn, G.; Bux, S.; Fleurial, J.-P.; Snyder, G. J. Thermoelectric Properties and Electronic Structure of the Zintl Phase Sr₅In₂Sb₆ and the Ca_{5-x}Sr_xIn₂Sb₆ Solid Solution. *J. Phys.: Condens. Matter* **2015**, 27 (1), 015801.
- (38) Aydemir, U.; Zevalkink, A.; Ormeci, A.; Wang, H.; Ohno, S.; Bux, S.; Snyder, G. J. Thermoelectric Properties of the Zintl Phases Yb₅M₂Sb₆ (M = Al, Ga, In). Dalton Trans. **2015**, 44 (15), 6767–6774.
- (39) Chanakian, S.; Zevalkink, A.; Aydemir, U.; Gibbs, Z. M.; Pomrehn, G.; Fleurial, J.-P.; Bux, S.; Snyder, G. J. Enhanced

- Thermoelectric Properties of Sr₅In₂Sb₆ via Zn-Doping. *J. Mater. Chem. A* **2015**, 3 (19), 10289–10295.
- (40) Aydemir, U.; Zevalkink, A.; Ormeci, A.; Gibbs, Z. M.; Bux, S.; Snyder, G. J. Thermoelectric Enhancement in BaGa₂Sb₂ by Zn Doping. *Chem. Mater.* **2015**, 27 (5), 1622–1630.
- (41) Ortiz, B. R.; Gorai, P.; Krishna, L.; Mow, R.; Lopez, A.; McKinney, R.; Stevanović, V.; Toberer, E. S. Potential for High Thermoelectric Performance in *n*-Type Zintl Compounds: A Case Study of Ba Doped KAlSb₄. *J. Mater. Chem. A* **2017**, 5 (8), 4036–4046.
- (42) Ortiz, B. R.; Gorai, P.; Stevanović, V.; Toberer, E. S. Thermoelectric Performance and Defect Chemistry in *n*-Type Zintl KGaSb₄. *Chem. Mater.* **2017**, 29 (10), 4523–4534.
- (43) Ortiz, B. R.; Gorai, P.; Braden, T.; Bensen, E. A.; Wilson, S. D.; Stevanović, V.; Toberer, E. S. Discovery of *n*-Type Zintl Phases RbAlSb₄, RbGaSb₄, CsAlSb₄, and CsGaSb₄. *ACS Appl. Energy Mater.* **2020**, 3 (3), 2182–2191.
- (44) Bux, S. K.; Zevalkink, A.; Janka, O.; Uhl, D.; Kauzlarich, S.; Snyder, J. G.; Fleurial, J.-P. Glass-like Lattice Thermal Conductivity and High Thermoelectric Efficiency in Yb₉Mn_{4.2}Sb₉. *J. Mater. Chem. A* **2014**, 2 (1), 215–220.
- (45) Ohno, S.; Zevalkink, A.; Takagiwa, Y.; Bux, S. K.; Snyder, G. J. Thermoelectric Properties of the Yb₉Mn_{4.2-x}Zn_xSb₉ Solid Solutions. *J. Mater. Chem. A* **2014**, 2 (20), 7478–7483.
- (46) Ohno, S.; Aydemir, U.; Amsler, M.; Pöhls, J.-H.; Chanakian, S.; Zevalkink, A.; White, M. A.; Bux, S. K.; Wolverton, C.; Snyder, G. J. Achieving ZT > 1 in Inexpensive Zintl Phase Ca₉Zn_{4+x}Sb₉ by Phase Boundary Mapping. *Adv. Funct. Mater.* **2017**, *27* (20), 1606361.
- (47) Wang, Y.; Bobev, S. Rare-Earth Metal Substitutions in $Ca_{9-x}RE_xMn_4Sb_9$ (RE = La-Nd, Sm; $x \approx 1$). Synthesis and Characterization of a New Series of Narrow-Gap Semiconductors. *Chem. Mater.* **2018**, *30* (10), 3518–3527.
- (48) Zevalkink, A.; Swallow, J.; Snyder, G. J. Thermoelectric Properties of Mn-Doped Ca₅Al₂Sb₆. *J. Electron. Mater.* **2012**, 41 (5), 813–818.
- (49) He, A.; Bux, S. K.; Hu, Y.; Uhl, D.; Li, L.; Donadio, D.; Kauzlarich, S. M. Structural Complexity and High Thermoelectric Performance of the Zintl Phase: Yb₂₁Mn₄Sb₁₈. *Chem. Mater.* **2019**, 31 (19), 8076–8086.
- (50) Chanakian, S.; Uhl, D.; Neff, D.; Drymiotis, F.; Park, J.; Petkov, V.; Zevalkink, A.; Bux, S. Exceptionally High Electronic Mobility in Defect-Rich Eu₂ZnSb_{2-x}Bi_x Alloys. *J. Mater. Chem. A* **2020**, 8 (12), 6004–6012.
- (51) Deller, K.; Eisenmann, B. Zur Kenntnis von Ca₁₁Sb₁₀ Und Ca₁₁Bi₁₀. Z. Naturforsch., B: J. Chem. Sci. **1976**, 31 (1), 29–34.
- (\$2) Brechtel, E.; Cordier, G.; Schäfer, H. Neue Verbindungen Mit Der Ca₉Mn₄Bi₉-Struktur: Zur Kenntnis von Ca₉Cd₄Bi₉, Sr₉Cd₄Bi₉ Und Ca₉Zn₄Sb₉. Z. Naturforsch., B: J. Chem. Sci. **1981**, 36 (9), 1099–1104.
- (53) Bobev, S.; Thompson, J. D.; Sarrao, J. L.; Olmstead, M. M.; Hope, H.; Kauzlarich, S. M. Probing the Limits of the Zintl Concept: Structure and Bonding in Rare-Earth and Alkaline-Earth Zinc-Antimonides Yb₉Zn_{4+x}Sb₉ and Ca₉Zn_{4.5}Sb₉. *Inorg. Chem.* **2004**, 43 (16), 5044–5052.
- (54) Mewis, A. AB₂X₂-Verbindungen Im CaAl₂Si₂-Typ, IV [1] Zur Struktur Der Verbindungen CaZn₂Sb₂, CaCd₂Sb₂, SrZn₂Sb₂ Und SrCd₂Sb₂, Z. Naturforsch., B: J. Chem. Sci. **1978**, 33 (4), 382–384.
- (55) Baranets, S.; Bobev, S. From the Ternary Phase $Ca_4Zn_{1+\delta}Sb_{11}$ ($\delta \approx 0.4$) to the Quaternary Solid Solutions $Ca_{14-x}RE_xZnSb_{11}$ (RE = La-Nd, Sm, Gd, $x \approx 0.9$). A Tale of Electron Doping via Rare-Earth Metal Substitutions and the Concomitant Structural Transformations. *Inorg. Chem.* **2019**, 58 (13), 8506–8516.
- (56) Petříček, V.; Dušek, M.; Palatinus, L. Crystallographic Computing System JANA2006: General Features. *Z. Kristallogr. Cryst. Mater.* **2014**, 229 (5), 345–352.
- (57) SAINT; Bruker AXS Inc., Madison, Wisconsin, USA, 2014.
- (58) SADABS; Bruker AXS Inc., Madison, Wisconsin, USA, 2014.

- (59) Sheldrick, G. M. SHELXT Integrated Space-Group and Crystal-Structure Determination. Acta Crystallogr., Sect. A: Found. Adv. 2015, 71 (1), 3–8.
- (60) Sheldrick, G. M. Crystal Structure Refinement with SHELXL. Acta Crystallogr., Sect. C: Struct. Chem. 2015, 71 (1), 3-8.
- (61) Gelato, L. M.; Parthé, E. STRUCTURE TIDY a Computer Program to Standardize Crystal Structure Data. J. Appl. Crystallogr. 1987, 20 (2), 139–143.
- (62) Kresse, G.; Furthmüller, J. Efficient Iterative Schemes for Ab Initio Total-Energy Calculations Using a Plane-Wave Basis Set. *Phys. Rev. B: Condens. Matter Mater. Phys.* **1996**, 54 (16), 11169–11186.
- (63) Perdew, J. P.; Burke, K.; Ernzerhof, M. Generalized Gradient Approximation Made Simple. *Phys. Rev. Lett.* **1996**, 77 (18), 3865–3868.
- (64) Jepsen, O.; Andersen, O. K. *The Stuttgart TB-LMTO-ASA Program*, Version 4.7; Max-Planck-Institut für Festkörperforschung: Stuttgart, Germany.
- (65) von Barth, U.; Hedin, L. A Local Exchange-Correlation Potential for the Spin Polarized Case: I. J. Phys. C: Solid State Phys. 1972, 5 (13), 1629–1642.
- (66) Steinberg, S.; Dronskowski, R. The Crystal Orbital Hamilton Population (COHP) Method as a Tool to Visualize and Analyze Chemical Bonding in Intermetallic Compounds. *Crystals* **2018**, *8* (5), 225
- (67) Ramadan, A. A.; Gould, R. D.; Ashour, A. On the Van Der Pauw Method of Resistivity Measurements. *Thin Solid Films* **1994**, 239 (2), 272–275.
- (68) Iwanaga, S.; Toberer, E. S.; LaLonde, A.; Snyder, G. J. A High Temperature Apparatus for Measurement of the Seebeck Coefficient. *Rev. Sci. Instrum.* **2011**, 82 (6), 063905.
- (69) Kanatzidis, M. G.; Pöttgen, R.; Jeitschko, W. The Metal Flux: A Preparative Tool for the Exploration of Intermetallic Compounds. *Angew. Chem., Int. Ed.* **2005**, 44 (43), 6996–7023.
- (70) Ovchinnikov, A.; Bobev, S. Bismuth as a Reactive Solvent in the Synthesis of Multicomponent Transition-Metal-Bearing Bismuthides. *Inorg. Chem.* **2020**, *59* (6), 3459–3470.
- (71) Ortiz, B. R.; Gomes, L. C.; Morey, J. R.; Winiarski, M.; Bordelon, M.; Mangum, J. S.; Oswald, I. W. H.; Rodriguez-Rivera, J. A.; Neilson, J. R.; Wilson, S. D.; Ertekin, E.; McQueen, T. M.; Toberer, E. S. New Kagome Prototype Materials: Discovery of KV₃Sb₅, RbV₃Sb₅, and CsV₃Sb₅. *Phys. Rev. Mater.* **2019**, 3 (9), 094407.
- (72) Sturza, M. I.; Amigó, M. L.; Facio, J. I.; Caglieris, F.; Aswartham, S.; Seiro, S.; Hess, C.; van den Brink, J.; Wurmehl, S.; Büchner, B. $La_6Pd_{2+x}Sb_{15}$ (x=0.28): A Rare-Earth Palladium Intermetallic Compound with Extended Pnictogen Ribbons. *J. Solid State Chem.* **2020**, *291*, 121578.
- (73) Xin, J.; Li, G.; Auffermann, G.; Borrmann, H.; Schnelle, W.; Gooth, J.; Zhao, X.; Zhu, T.; Felser, C.; Fu, C. Growth and Transport Properties of Mg_3X_2 (X = Sb, Bi) Single Crystals. *Mater. Today Phys.* **2018**, *7*, 61–68.
- (74) Imasato, K.; Fu, C.; Pan, Y.; Wood, M.; Kuo, J. J.; Felser, C.; Snyder, G. J. Metallic *n*-Type Mg₃Sb₂ Single Crystals Demonstrate the Absence of Ionized Impurity Scattering and Enhanced Thermoelectric Performance. *Adv. Mater.* **2020**, 32 (16), 1908218.
- (75) Ovchinnikov, A.; Bobev, S. On the Effect of Ga and In Substitutions in the Ca₁₁Bi₁₀ and Yb₁₁Bi₁₀ Bismuthides Crystallizing in the Tetragonal Ho₁₁Ge₁₀ Structure Type. *Acta Crystallogr., Sect. C: Struct. Chem.* **2018**, 74 (3), 269–273.
- (76) Brown, S. R.; Kauzlarich, S. M.; Gascoin, F.; Snyder, G. J. High-Temperature Thermoelectric Studies of $A_{11}{\rm Sb}_{10}$ ($A={\rm Yb,\,Ca}$). J. Solid State Chem. **200**7, 180 (4), 1414–1420.
- (77) Bärnighausen, H. Group-Subgroup Relations between Space Groups: A Useful Tool in Crystal Chemistry. *Commun. Math. Comput. Chem.* **1980**, *9*, 139–175.
- (78) Cordier, G.; Schäfer, H.; Stelter, M. Ca₁₁InSb₉, Eine Zintlphase Mit Diskreten InSb₄⁹ Anionen. Z. Naturforsch., B: J. Chem. Sci. **1985**, 40 (7), 868–871.

- (79) Xia, S.; Hullmann, J.; Bobev, S.; Ozbay, A.; Nowak, E. R.; Fritsch, V. Synthesis, Crystal Structures, Magnetic and Electric Transport Properties of Eu₁₁InSb₉ and Yb₁₁InSb₉. *J. Solid State Chem.* **2007**, *180* (7), 2088–2094.
- (80) Hullmann, J.; Xia, S.-Q.; Bobev, S. Sr₁₁InSb₉ Grown from Molten In. *Acta Crystallogr., Sect. E: Struct. Rep. Online* **2007**, 63 (9), No. i178.
- (81) Yi, T.; Cox, C. A.; Toberer, E. S.; Snyder, G. J.; Kauzlarich, S. M. High-Temperature Transport Properties of the Zintl Phases Yb₁₁GaSb₉ and Yb₁₁InSb₉. *Chem. Mater.* **2010**, 22 (3), 935–941.
- (82) Kastbjerg, S.; Uvarov, C. A.; Kauzlarich, S. M.; Chen, Y.-S.; Nishibori, E.; Spackman, M. A.; Iversen, B. B. Crystal Structure and Chemical Bonding of the Intermetallic Zintl Phase Yb₁₁AlSb₉. *Dalton Trans.* **2012**, *41* (34), 10347–10353.
- (83) Ganguli, A. K.; Gupta, S.; Corbett, J. D. New Tetragonal Structure Type for A_2 Ca₁₀Sb₉ (A = Li, Mg). Electronic Variability around a Zintl Phase. *Inorg. Chem.* **2006**, 45 (1), 196–200.
- (84) Wang, A.; Baranets, S.; Liu, Y.; Tong, X.; Stavitski, E.; Zhang, J.; Chai, Y.; Yin, W.-G.; Bobev, S.; Petrovic, C. Magnetic Mixed Valent Semimetal EuZnSb₂ with Dirac States in the Band Structure. *Phys. Rev. Res.* **2020**, 2 (3), 033462.
- (85) Holm, A. P.; Ozawa, T. C.; Kauzlarich, S. M.; Morton, S. A.; Dan Waddill, G.; Tobin, J. G. X-Ray Photoelectron Spectroscopy Studies of Yb₁₄MnSb₁₁ and Yb₁₄ZnSb₁₁. *J. Solid State Chem.* **2005**, *178* (1), 262–269.
- (86) Saparov, B.; Bobev, S.; Ozbay, A.; Nowak, E. R. Synthesis, Structure and Physical Properties of the New Zintl Phases Eu₁₁Zn₆Sb₁₂ and Eu₁₁Cd₆Sb₁₂. *J. Solid State Chem.* **2008**, *181* (10), 2690–2696.
- (87) Suen, N.-T.; Wang, Y.; Bobev, S. Synthesis, Crystal Structures, and Physical Properties of the New Zintl Phases A_{21} Zn₄Pn₁₈ (A =Ca, Eu; Pn =As, Sb)—Versatile Arrangements of [ZnPn₄] Tetrahedra. J. Solid State Chem. **2015**, 227, 204–211.
- (88) Kim, H.; Huang, Q.; Lynn, J. W.; Kauzlarich, S. M. Neutron Diffraction Study of the Ternary Transition Metal Zintl Compound Ca₁₄MnSb₁₁. *J. Solid State Chem.* **2002**, *168* (1), 162–168.
- (89) Holm, A. P.; Olmstead, M. M.; Kauzlarich, S. M. The Crystal Structure and Magnetic Properties of a New Ferrimagnetic Semi-conductor: Ca₂₁Mn₄Sb₁₈. *Inorg. Chem.* **2003**, *42* (6), 1973–1981.
- (90) Xia, S.-Q.; Bobev, S. Cation-Anion Interactions as Structure Directing Factors: Structure and Bonding of Ca₂CdSb₂ and Yb₂CdSb₃. *J. Am. Chem. Soc.* **2007**, *129* (13), 4049–4057.
- (91) Bridges, C. A.; Krishnamurthy, V. V.; Poulton, S.; Paranthaman, M. P.; Sales, B. C.; Myers, C.; Bobev, S. Magnetic Order in CaMn₂Sb₂ Studied via Powder Neutron Diffraction. *J. Magn. Magn. Mater.* **2009**, 321 (22), 3653–3657.
- (92) Prakash, J.; Stoyko, S.; Voss, L.; Bobev, S. On the Extended Series of Quaternary Zintl Phases Ca₁₃REMnSb₁₁ (RE = La-Nd, Sm, Gd-Dy). Eur. J. Inorg. Chem. **2016**, 2016 (18), 2912–2922.
- (93) Xia, S.-Q.; Bobev, S. Diverse Polyanions Based on $MnBi_4$ and $MnSb_4$ Tetrahedra: Polymorphism, Structure, and Bonding in $Ca_{21}Mn_4Bi_{18}$ and $Ca_{21}Mn_4Sb_{18}$. Inorg. Chem. 2007, 46 (3), 874–883.
- (94) Cox, C. A.; Toberer, E. S.; Levchenko, A. A.; Brown, S. R.; Snyder, G. J.; Navrotsky, A.; Kauzlarich, S. M. Structure, Heat Capacity, and High-Temperature Thermal Properties of Yb₁₄Mn_{1-x}Al_xSb₁₁. *Chem. Mater.* **2009**, *21* (7), 1354–1360.
- (95) Xia, S.-Q.; Bobev, S. New Manganese-Bearing Antimonides and Bismuthides with Complex Structures. Synthesis, Structural Characterization, and Electronic Properties of $Yb_9Mn_{4+x}Pn_9$ (Pn = Sb or Bi). *Chem. Mater.* **2010**, 22 (3), 840–850.
- (96) Rauscher, J. F.; Cox, C. A.; Yi, T.; Beavers, C. M.; Klavins, P.; Toberer, E. S.; Snyder, G. J.; Kauzlarich, S. M. Synthesis, Structure, Magnetism, and High Temperature Thermoelectric Properties of Ge Doped Yb₁₄MnSb₁₁. *Dalton Trans.* **2010**, 39 (4), 1055–1062.
- (97) Grebenkemper, J. H.; Klemenz, S.; Albert, B.; Bux, S. K.; Kauzlarich, S. M. Effects of Sc and Y Substitution on the Structure and Thermoelectric Properties of Yb₁₄MnSb₁₁. *J. Solid State Chem.* **2016**, 242, 55–61.

- (98) Kim, H.; Condron, C. L.; Holm, A. P.; Kauzlarich, S. M. Synthesis, Structure, and Magnetic Properties of a New Ternary Zintl Phase: $Sr_{21}Mn_4Sb_{18}$. *J. Am. Chem. Soc.* **2000**, 122 (43), 10720–10721. (99) Ovchinnikov, A.; Saparov, B.; Xia, S.-Q.; Bobev, S. The Ternary Alkaline-Earth Metal Manganese Bismuthides Sr_2MnBi_2 and $Ba_2Mn_{1-x}Bi_2$ ($x \approx 0.15$). *Inorg. Chem.* **2017**, 56 (20), 12369–12378. (100) Toberer, E. S.; Brown, S. R.; Ikeda, T.; Kauzlarich, S. M.; Snyder, G. J. High Thermoelectric Efficiency in Lanthanum Doped Yb₁₄MnSb₁₁. *Appl. Phys. Lett.* **2008**, 93 (6), 062110.
- (101) Ovchinnikov, A.; Darone, G.; Saparov, B.; Bobev, S. Exploratory Work in the Quaternary System of Ca–Eu–Cd–Sb: Synthesis, Crystal, and Electronic Structures of New Zintl Solid Solutions. *Materials* **2018**, *11* (11), 2146.
- (102) Childs, A. B.; Baranets, S.; Bobev, S. Five New Ternary Indium-Arsenides Discovered. Synthesis and Structural Characterization of the Zintl Phases Sr₃In₂As₄, Ba₃In₂As₄, Eu₃In₂As₄, Sr₅In₂As₆ and Eu₅In₂As₆. *J. Solid State Chem.* **2019**, 278, 120889.
- (103) Balvanz, A.; Baranets, S.; Bobev, S. Synthesis and Structural Characterization of the New Zintl Phases Ba₃Cd₂P₄ and Ba₂Cd₂P₃. Rare Example of Small Gap Semiconducting Behavior with Negative Thermopower within the Range 300 K–700 K. *J. Solid State Chem.* **2020**, 289, 121476.
- (104) Perez, C. J.; Wood, M.; Ricci, F.; Yu, G.; Vo, T.; Bux, S. K.; Hautier, G.; Rignanese, G.-M.; Snyder, G. J.; Kauzlarich, S. M. Discovery of Multivalley Fermi Surface Responsible for the High Thermoelectric Performance in Yb₁₄MnSb₁₁ and Yb₁₄MgSb₁₁. *Sci. Adv.* **2021**, *7* (4), No. eabe9439.
- (105) Xu, J.; Kleinke, H. Unusual Sb-Sb Bonding in High Temperature Thermoelectric Materials. *J. Comput. Chem.* **2008**, 29 (13), 2134–2143.
- (106) Kleinke, H. Stabilization of the New Antimonide $Zr_2V_6Sb_9$ by V–V and Sb–Sb Bonding. *Eur. J. Inorg. Chem.* **1998**, *1998* (9), 1369–1375.
- (107) Kleinke, H. Sb-Sb Interactions in the Hafnium-Rich Antimonide Hf_6TiSb_4 . *Inorg. Chem.* **1999**, 38 (12), 2931–2935.
- (108) Kleinke, H. From Molecular Sb Units to Infinite Chains, Layers, and Networks: Sb–Sb Interactions in Metal-Rich Antimonides. *Chem. Soc. Rev.* **2000**, 29 (6), 411–418.
- (109) Elder, I.; Lee, C.-S.; Kleinke, H. Zr₁₁Sb₁₈: A New Binary Antimonide Exhibiting an Unusual Sb Atom Network with Nonclassical Sb-Sb Bonding. *Inorg. Chem.* **2002**, *41* (3), 538–545.
- (110) Mills, A. M.; Mar, A. Layered Rare-Earth Gallium Antimonides REGaSb₂ (RE = La-Nd, Sm). J. Am. Chem. Soc. **2001**, 123 (6), 1151–1158.
- (111) Mills, A. M.; Deakin, L.; Mar, A. Electronic Structures and Properties of $RE_{12}Ga_4Sb_{23}$ (RE = La-Nd, Sm) and Superconducting $La_{13}Ga_8Sb_{21}$. Chem. Mater. **2001**, 13 (5), 1778–1788.
- (112) Mills, A. M.; Lam, R.; Ferguson, M. J.; Deakin, L.; Mar, A. Chains, Planes, and Antimonides. *Coord. Chem. Rev.* **2002**, 233–234, 207–222.
- (113) Moore, S. H. D.; Deakin, L.; Ferguson, M. J.; Mar, A. Physical Properties and Bonding in RE_3TiSb_5 (RE = La, Ce, Pr, Nd, Sm). Chem. Mater. **2002**, 14 (11), 4867–4873.
- (114) Heremans, J. P.; Jovovic, V.; Toberer, E. S.; Saramat, A.; Kurosaki, K.; Charoenphakdee, A.; Yamanaka, S.; Snyder, G. J. Enhancement of Thermoelectric Efficiency in PbTe by Distortion of the Electronic Density of States. *Science* **2008**, *321* (5888), 554–557.
- (115) Devlin, K. P.; Grebenkemper, J. H.; Lee, K.; Cerretti, G.; Bux, S. K.; Kauzlarich, S. M. Enhancement of the Thermal Stability and Thermoelectric Properties of Yb₁₄MnSb₁₁ by Ce Substitution. *Chem. Mater.* **2020**, 32 (21), 9268–9276.
- (116) Adachi, K. Magnetic Anisotropy Energy in Nickel Arsenide Type Crystals. J. Phys. Soc. Jpn. 1961, 16 (11), 2187–2206.
- (117) Tamaki, H.; Sato, H. K.; Kanno, T. Isotropic Conduction Network and Defect Chemistry in Mg_{3+δ}Sb₂-Based Layered Zintl Compounds with High Thermoelectric Performance. *Adv. Mater.* **2016**, 28 (46), 10182–10187.

- (118) Cahill, D. G.; Watson, S. K.; Pohl, R. O. Lower Limit to the Thermal Conductivity of Disordered Crystals. *Phys. Rev. B: Condens. Matter Mater. Phys.* **1992**, 46 (10), 6131–6140.
- (119) Toberer, E. S.; Zevalkink, A.; Snyder, G. J. Phonon Engineering Through Crystal Chemistry. *J. Mater. Chem.* **2011**, *21* (40), 15843–15852.
- (120) Baranets, S.; Ovchinnikov, A.; Bobev, S. Complex Structural Disorder in the Zintl Phases Yb₁₀MnSb₉ and Yb₂₁Mn₄Sb₁₈. *Inorg. Chem.* **2021**, DOI: 10.1021/acs.inorgchem.0c00519b, in print.